Research Square

Preprints are preliminary reports that have not undergone peer review.
They should not be considered conclusive, used to inform clinical practice,
or referenced by the media as validated information.

Selective coupling of the Western Tibetan Vortex and the South Asian High

Xiao-Feng Li

lixf87@mail.sysu.edu.cn

Sun Yat-Sen University (Zhuhai Campus)

Hayley J. Fowler

Newcastle University

Song Yang

Sun Yat-Sen University (Zhuhai Campus)

Binbo Lei

Sun Yat-Sen University (Zhuhai Campus)

Yonglu Li

Sun Yat-Sen University (Zhuhai Campus)

Article

Keywords: Western Tibetan Vortex, South Asian High, subtropical westerly jet, Karakoram Zonal Index, northern Indian Ocean, Tibetan Plateau

Posted Date: November 10th, 2026

DOI: https://doi.org/10.21203/rs.3.rs-11482186/v1

License: This work is licensed under a Creative Commons Attribution 4.0 International License.
Read Full License

Additional Declarations: No competing interests reported.

Selective coupling of the Western Tibetan Vortex and the South Asian High

Xiao-Feng Li[1,*] , Hayley J. Fowler[2], Song Yang[1], Binbo Lei[1], Yonglu Li[1]

1. *School of Atmospheric Sciences, Sun Yat-sen University & Southern Marine Science and Engineering Guangdong Laboratory (Zhuhai) & Guangdong Province Key Laboratory for Climate Change and Natural Disaster Studies, Zhuhai 519000, China*
2. *School of Engineering, Newcastle University, Newcastle upon Tyne NE1 7RU, UK*

Target journal: npj Climate and Atmospheric Science (Article).

Corresponding author address: Dr. Xiao-Feng Li, Meteorology Department, School of Atmospheric Sciences, Sun Yat-Sen University (Zhuhai Campus), Zhuhai 519082, Guangdong, China. E-mail: lixf87@mail.sysu.edu.cn.

Abstract

The Western Tibetan Vortex (WTV) and South Asian High (SAH) overlap in the Asian upper troposphere, but whether they represent distinct phenomena and how they interact remain unclear. Using ERA5 reanalysis (1979–2023) and 53 CMIP6 models, we demonstrate that the WTV is a year-round circulation-variability mode distinct from the summer SAH anticyclone. Their summer variability is selectively coupled through SAH position rather than intensity or extent, with SAH centre displacements explaining 52.8% of WTV variance. This relationship involves two complementary pathways: meridional displacement associated with subtropical westerly jet shifts and zonal displacement associated with circulation anomalies over the western Tibetan Plateau. We further show that WTV variability covaries with the continuous western ridge of the SAH, but not with intermittent splitting into separate centres. Most CMIP6 models reproduce the coupling structure but underestimate its strength. These findings clarify the dynamical relationship between two distinct atmospheric phenomena and resolve a longstanding ambiguity surrounding the SAH western centre.

Keywords: Western Tibetan Vortex; South Asian High; subtropical westerly jet; Karakoram Zonal Index; northern Indian Ocean; Tibetan Plateau

1. Introduction

The upper-tropospheric circulation over the Tibetan Plateau and its surroundings strongly influences Asian climate, from monsoon rainfall over South and East Asia to glacier mass balance in the Karakoram. Two prominent features of this circulation, the South Asian High (SAH) and the Western Tibetan Vortex (WTV), have largely been studied in parallel. The SAH is a persistent summer anticyclonic circulation in the upper troposphere, traditionally identified from the geopotential-height field near 100 hPa (Tao and Zhu, 1964; Krishnamurti et al., 1973). The WTV, in contrast, denotes a dominant mode of circulation variability over the western Tibetan Plateau, represented by the leading EOF pattern and quantified by the Karakoram Zonal Index (KZI) from the 200-hPa zonal-wind dipole (Forsythe et al., 2017; Li et al., 2018; Wang et al., 2023). Thus, the SAH and the WTV represent fundamentally different circulation concepts: the former is a circulation system identified directly from the atmospheric field, whereas the latter is a mode of circulation variability. Whether WTV variability simply represents the western-flank expression of SAH variability or constitutes a distinct mode coupled to the SAH has not been examined systematically.

The SAH is a thermally driven system maintained by sensible heating over the Tibetan Plateau and latent heating associated with the Asian summer monsoon, rather than by the descending branch of the Hadley circulation (Hoskins and Rodwell, 1995; Rodwell and Hoskins, 1996; Liu and Wu, 2004; Wu et al., 2007, 2012; Liu et al., 2013; Zhang et al., 2016). Its characteristic summer structure is strongly seasonally confined: the 16,720 gpm contour at 100 hPa, widely used to depict the SAH (Huang et al., 2011) occurs only from June to September. SAH variability is characterised by indices of intensity, area, centre position, ridge line and boundary latitudes. Both zonal and meridional displacements of the SAH have important climatic associations: Its zonal (east-west) displacement, traditionally described as the Tibetan-mode/Iranian-mode oscillation (Zhang et al., 2002), is linked to drought and flood anomalies over the Yangtze basin (Zhang and Wu, 2001). Its meridional (north-south) displacement is associated with Indian and East Asian monsoon rainfall (Wei et al., 2015). The SAH is also strongly influenced by tropical Indian Ocean warming which strengthens the SAH and shifts it equatorward (Huang et al., 2011; Qu and Huang, 2012), and the preceding winter El Niño–Southern Oscillation (ENSO) modulates it through the Indian Ocean capacitor effect (Xie et al., 2009; Xue et al., 2015). The SAH is also tightly coupled to the subtropical westerly jet (SWJ) whose axis lies along its northern flank, and covaries with its seasonal migration and interannual displacement (Lin and Lu, 2005; Liu et al., 2010; Wei et al., 2017). The SAH is also linked to the circumglobal teleconnection (CGT), which propagates along the jet waveguide: the Indian summer monsoon heating that likewise forces the SAH (Hoskins and Rodwell, 1995) excites the CGT wave

train, whose main action centre near South Asia lies over west-central Asia (35–40°N, 60–70°E), just northwest of the high (Ding and Wang, 2005).

Research on the WTV has developed more recently and largely separately from that on the SAH. The WTV was first identified by Forsythe et al. (2017) and subsequently characterized systematically by Li et al. (2018). Forsythe et al. (2017) showed that a vortex-like circulation pattern near the western end of the plateau modulates Karakoram temperature and glacial melt, while Li et al. (2018) documented its spatial structure and seasonal-to-interannual variability. They introduced the KZI to quantify its strength from the meridional difference in 200 hPa zonal wind across the plateau. Unlike the strongly seasonal SAH, the WTV occurs in all seasons, has a deep quasi-barotropic structure and is inconsistent with a thermally direct circulation (Li et al., 2022). Conversely, the WTV strongly modulates plateau air temperature through adiabatic and cloud-radiative processes (Li et al., 2019; Wang et al., 2026b). The WTV is the leading mode (EOF1) of wind variability over the western Tibetan Plateau in most seasons (Wang et al., 2023) and has been linked to near-surface temperature, precipitation, ozone, and spring snow cover (Li et al., 2018; Li et al., 2019; Li et al., 2022; Wang et al., 2025). The external drivers identified to date are predominantly remote and dynamical rather than local and thermal: the position and intensity of the subtropical jet (Li et al., 2018), autumn ENSO acting through the Indian Ocean Walker circulation (Jiang et al., 2025), and the summer North Atlantic Oscillation (NAO) acting through eastward Rossby wave propagation (Lei et al., 2025).

Despite their spatial overlap and their common association with the upper-tropospheric circulation over the Tibetan Plateau, the WTV and SAH have been studied largely in parallel, and their relationship has not been systematically quantified. Three considerations make this relationship particularly important. First, the southern box used to define the KZI (20–32.5°N) overlaps the tropical easterlies on the southern flank of the summer SAH, raising the possibility that the KZI incorporates an SAH-related component into the measured WTV variability. Second, the WTV emerges in summer as the leading mode (EOF1) of wind variability over the western Tibetan Plateau, with its largest seasonal variance contribution (45.78%; Wang et al., 2023). The corresponding EOF1 exhibits a more complete anticyclonic-cyclonic circulation structure than is captured by the fixed-lobe KZI, indicating that the KZI represents only part of the full WTV variability. Third, a companion study on WTV predictability (Li et al., 2026, submitted; hereafter the companion study) identifies a pathway linking northern Indian Ocean (NIO) warming, southward expansion of the SAH, southward displacement of the jet axis, and weakening of the WTV. This raises a fundamental question: does the WTV

represent a distinct circulation-variability mode that is coupled to SAH variability, or is it primarily a projection of variability in the SAH's western flank?

Here, we address this question by placing the SAH and WTV within a common diagnostic framework. Using the ERA5 reanalysis for 1979–2023 and historical simulations from 53 CMIP6 models, we quantify SAH circulation and WTV variability within a common temporal framework and address three questions:

(Q1) What is the relationship between SAH circulation and WTV variability?

(Q2) Which properties of the SAH are coupled to WTV variability, and what role does the subtropical jet play in this coupling?

(Q3) Are the observed coupling relationships robust across climate models?

We use this framework to distinguish structural overlap from dynamical coupling and to determine whether any observed relationship is specific to SAH position, amplitude, or extent. We find that the WTV is a distinct mode of variability, coupled selectively to SAH position through a jet-mediated meridional pathway and a direct zonal pathway. These links hold across the CMIP6 models. The framework also clarifies the contested western centre of the SAH and provides a WTV index with the SAH-displacement component removed for applications.

2. Data and methods

2.1. Data and statistical analysis

We use monthly mean pressure-level zonal and meridional wind, air temperature and geopotential from the ERA5 reanalysis at 0.25° horizontal resolution for 1979–2023 (Hersbach et al., 2020). Geopotential is converted to geopotential height (HGT) by dividing by 9.80665 m s^{-2}. The reliability of ERA5 in depicting year-to-year surface air temperature variability over the Tibetan Plateau has been documented previously (Wang et al., 2026a). Sea surface temperature (SST) is obtained from NOAA Extended Reconstructed SST version 6 (ERSSTv6; Huang et al., 2025a, b) at 2° horizontal resolution. For model evaluation we use historical simulations from 53 CMIP6 models (Eyring et al., 2016) for 1979–2014, regridded to a common 0.75° grid (details in Table S1).

All seasonal time series are linearly detrended across years before statistical analysis, separately for each variable, index and model, and the same detrending is applied in the monthly per-calendar-month analyses. We use Pearson correlation, partial correlation, and ordinary least-squares (OLS) multiple regression. Model explanatory power is quantified using the coefficient of determination (R^2); the unique contribution of an additional predictor is quantified

as the increase in explained variance ($\triangle R^2$) when that predictor is added to the regression model (Wilks, 2011). The reported R^2 values refer to variance explained within the analysed sample. Statistical mediation is assessed using the product-of-coefficients approach (Baron and Kenny, 1986; Preacher and Hayes, 2008), as recently applied in climate-science research (Kolstad and O'Reilly, 2024). The indirect effect is estimated as the product of the predictor–mediator and mediator–outcome regression coefficients, with 95% confidence intervals obtained from 10,000 bootstrap resamples generated by resampling years with replacement (Efron, 1979). Because these diagnostics are based primarily on contemporaneous seasonal-mean relationships, the mediation analysis is interpreted as evidence of a statistical pathway rather than proof of causal direction. The statistical significance of Pearson correlations is assessed using a two-tailed Student's *t*-test; for correlations computed on pooled monthly samples, the degrees of freedom are adjusted for serial autocorrelation through an effective sample size (Bretherton et al., 1999). For families of related statistical tests, namely the SAH–WTV correlations of Section 4 and the western-ridge diagnostics of Section 6.1, we control the false discovery rate using the Benjamini–Hochberg procedure at $q = 0.05$. Where standardised series are used, each series is centred on its mean and divided by its standard deviation over the analysis period. The stability of the principal regression models is further verified by leave-one-out cross-validation (Section 5.2).

The primary observational analysis covers 1979–2023 (N=45 summers), whereas observation–CMIP6-model comparisons use the common 1979–2014 period (N=36 summers). Seasonal means are calculated from monthly means; unless otherwise stated, summer refers to June–August (JJA).

2.2. The Karakoram Zonal Index

Following Forsythe et al. (2017) and Li et al. (2018), the KZI is defined as the standardised difference in area-mean 200-hPa zonal-wind anomalies between a northern and a southern box flanking the Karakoram:

$$KZI = (U'_N - U'_S)/\sigma_0 \quad (1)$$

where U'_N and U'_S are the cosine-latitude-weighted area-mean 200-hPa zonal-wind anomalies over the northern (40–50°N, 52.5–86.25°E) and southern (20–32.5°N, 52.5–93.75°E) boxes, respectively, obtained by removing the 1982–2010 climatological monthly means, and σ_0 is the standard deviation of $U'_N - U'_S$ pooled over all months of that base period. Positive (negative) KZI values correspond to anticyclonic (cyclonic) WTV anomalies.

The KZI is therefore a signed anomaly index that quantifies the amplitude and sign of WTV variability. Its two-lobe 200 hPa zonal-wind dipole provides a fixed-index representation of the broader WTV circulation mode identified by EOF analysis (Wang et al., 2023). The EOF pattern and its PC1 characterize the spatial structure and temporal

variability of the data-derived mode, respectively, whereas the KZI provides a fixed, physically interpretable measure of that variability. Their correspondence is evaluated explicitly in Section 3.1.

2.3. SAH characteristic indices

In contrast to the WTV, which is represented by an anomaly index, the SAH is characterized directly from the geopotential-height field. The SAH centre is defined as the maximum geopotential height (HGT) within 10–45°N, 30–130°E. Its latitude and longitude are refined by parabolic interpolation around the grid-point maximum (a one-dimensional parabola fitted to the grid-point maximum and its two adjacent points, applied separately in latitude and longitude), and the corresponding maximum HGT is retained as a measure of centre height (Zhang et al., 2002; Qian et al., 2002). SAH centre position is diagnosed at 100 and 200 hPa, with 200 hPa used as the primary level for comparison with the wind-based KZI. The 150-hPa level is additionally examined in the western-ridge analysis in Section 6. For the centre-count analysis in Section 6, an additional local HGT maximum is identified as a coexisting centre when it is separated from the main centre by a minimum at least 10 gpm along the corresponding latitude circle. To quantify the western ridge in Section 6, we define a western–ridge contrast index (WRC) as the maximum geopotential height within a western box (10–45°N, 20–70°E) minus the maximum HGT within an eastern box (10–45°N, 75–125°E):

$$WRC = max(HGT_W) - max(HGT_E) \quad (2)$$

Taking the difference reduces the contribution of basin-wide SAH intensity variations and emphasizes variability in the relative prominence of the western ridge; larger WRC values therefore indicate a relatively stronger western ridge.

At 100 hPa, we additionally characterize the SAH using its 16,720 gpm contour, following the general contour-based approach of Huang et al. (2011). The southern and northern boundaries are defined as the southernmost and northernmost latitudes at which the maximum HGT across 40–100°E reaches or exceeds 16,720 gpm. SAH area is calculated from the cosine-weighted grid cells enclosed by the 16,720-gpm contour within 0–60°N, 0–150°E, the western and eastern boundary longitudes of the contour within 15–45°N. SAH intensity is defined here as the area-mean 100 hPa HGT over 20–35°N, 40–100°E. Because the 16,720 gpm contour is climatologically present only from June to September, these contour-based diagnostics are restricted to the SAH season; the main summer analysis uses JJA means. Centre position and intensity, which do not require the characteristic contour, can also be calculated outside this period. 200-hPa serves as the primary analysis level, matching the wind-based definition of the KZI, while the 100-hPa centre is provided as a measure of level-dependent sensitivity (Table 1).

Throughout the analysis, 'SAH–WTV coupling' refers to covariability between their temporal variations rather than similarity between their climatological structures. Because the fixed KZI boxes overlap the summer SAH circulation, we explicitly assess the contribution of SAH displacement to the KZI in Sections 3.2 and 6.3.

2.4. Subtropical westerly jet and Northern Indian Ocean (NIO) SST indices

The subtropical westerly jet (SWJ) is characterised from the 200-hPa zonal wind averaged over 40–100°E (Lin and Lu, 2005; Schiemann et al., 2009). The jet-axis latitude is defined as the latitude of maximum zonal wind within 20–60°N, and jet speed as the zonal wind at that latitude. For seasonal analyses, the maximum is identified from the JJA-mean meridional profile and refined by parabolic interpolation around the grid-point maximum. For monthly analyses the same procedure is applied separately to each monthly-mean profile. As a complementary measure that does not depend on locating the jet maximum, we also calculate the area-mean 200-hPa zonal wind over 30–50°N, 40–100°E. The northern Indian Ocean (NIO) SST index is defined as the cosine-latitude-weighted JJA-mean SST anomaly over 0–20°N, 50–100°E, following the companion study (Li et al., 2026). All jet and NIO indices are linearly detrended before statistical analysis, consistent with Section 2.1.

2.5. Summer-mean vorticity budget of the western-ridge composite

To diagnose the dynamical processes associated with western-ridge variability (Section 6), we evaluate the summer-mean relative-vorticity budget at 200 hPa and 100 hPa (Holton, 2004) using strong-minus-weak western-ridge composites. Strong and weak western-ridge summers are defined as the upper and lower terciles, respectively, of the detrended 200-hPa west-east HGT contrast defined in Section 2.3. Composite anomalies are calculated as the difference between the strong- and weak-ridge JJA-means, with15 summers in each group.

The composite relative-vorticity budget is written as:

$$-V' \cdot \nabla(\bar{\zeta} + f) - \bar{V} \cdot \nabla\zeta' - (\bar{\zeta} + f)\nabla \cdot V' - \zeta'\nabla \cdot \bar{V} - \bar{\omega}\frac{\partial \zeta'}{\partial p} - \omega'\frac{\partial \bar{\zeta}}{\partial p} + R' = 0 \quad (3)$$

Here, overbars ($\bar{}$) denote the 1979–2023 JJA climatological mean and primes ($'$) denote strong-minus-weak composite differences. The residual term, R', contains processes not explicitly represented in Eq. (3), including the local tendency, transient-eddy, nonlinear and frictional terms. The first term ($-V' \cdot \nabla(\bar{\zeta} + f)$) represents advection of the climatological absolute vorticity gradient by the composite wind anomaly, hereafter denoted MAINT. The second term ($-\bar{V} \cdot \nabla\zeta'$) represents advection of the composite relative-vorticity anomaly by the climatological flow, hereafter denoted PROP. The third and fourth terms ($-(\bar{\zeta} + f)\nabla \cdot V' - \zeta'\nabla \cdot \bar{V}$) together represent the divergence-stretching

contribution (STRETCH), of which the planetary part $-f\nabla \cdot V'$ (equivalent to $f\frac{\partial \omega'}{\partial p}$ by mass continuity) is the dominant component. The following two terms ($-\bar{\omega}\frac{\partial \zeta'}{\partial p} - \omega'\frac{\partial \bar{\zeta}}{\partial p}$) describe the vertical-advection contribution (VERT).

Vertical derivatives at 200 and 100 hPa are estimated using centred finite differences between 150-250 and 70-125 hPa, respectively. Each budget term is projected onto the composite vorticity anomaly over the western ridge box (25–45°N, 20–70°E), $\lambda = \langle term \cdot \zeta' \rangle / \langle \zeta'^2 \rangle$. A positive λ indicates that the is spatially aligned with the composite vorticity anomaly, whereas a negative λ indicates opposition to the anomaly (Feldstein, 2002). To estimate the component of MAINT associated with the WTV-related circulation, we repeat the calculation after replacing the full composite wind anomaly (V') with the wind anomaly reconstructed from its linear regression onto the KZI and scaled by the strong-minus-weak composite KZI difference.

3. Distinction and structural overlap between the WTV and the SAH

3.1. A circulation system and a variability mode

The SAH and WTV represent fundamentally different circulation concepts: the SAH is a circulation system identified directly from the atmospheric field, whereas the WTV is a mode of circulation variability over the western Tibetan Plateau. The SAH appears directly in the geopotential-height field as an upper-tropospheric anticyclone and is traditionally characterized near 100-hPa (Tao and Zhu, 1964; Krishnamurti et al., 1973; Figure 1a). Its summer state is characterised by its centre position, intensity, areal extent, and boundaries, including diagnostics based on the 16,720-gpm contour (Figure 1a). The WTV, in contrast, is identified as the leading EOF of detrended JJA 200-hPa horizontal-wind variability over 22–50°N, 50–92°E (Wang et al., 2023). The leading mode explains 40.1% of the total wind variance and exhibits a vortex-like circulation anomaly over the western Tibetan Plateau (Figure 1b). The fixed-box KZI provides an independent index-based measure of this variability. Its associated circulation pattern closely resembles EOF1, with spatial correlations of 0.90 within the EOF domain and 0.80 over the displayed domain (Figure 1c); PC1 and the KZI are also strongly correlated. Thus, the SAH diagnostics describe the state and geometry of an upper-tropospheric anticyclone, whereas the KZI describes the temporal amplitude and sign of a circulation-variability mode.

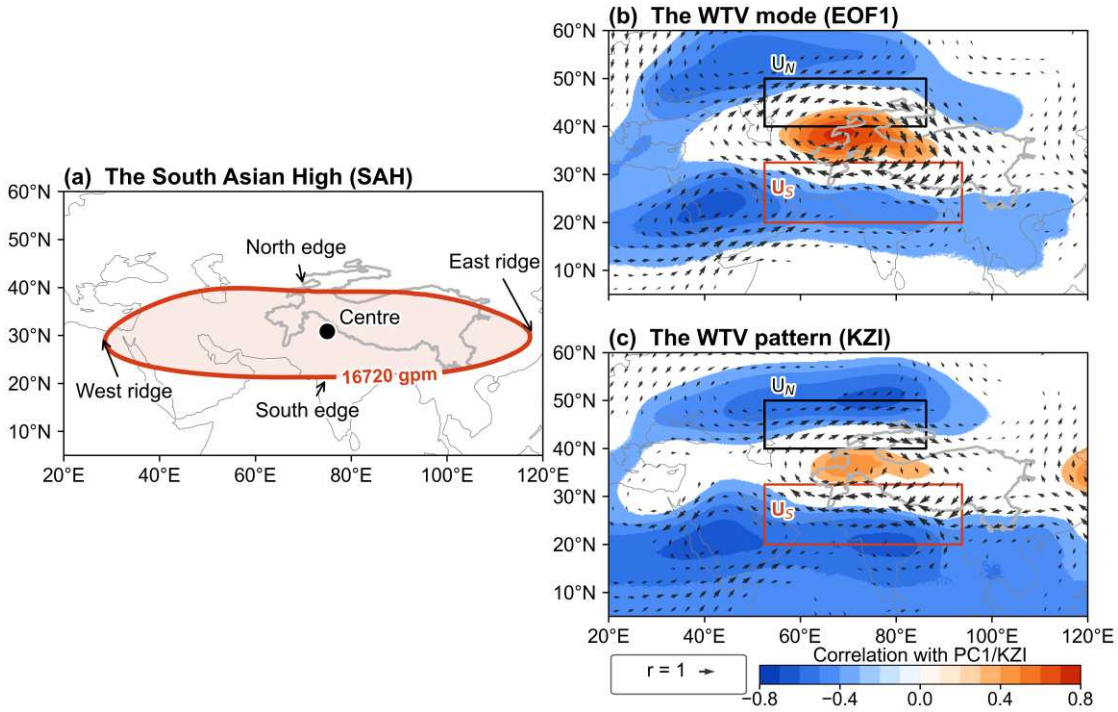


Figure 1. Distinction between the South Asian High (SAH) and Western Tibetan Vortex (WTV) in summer (JJA) during 1979–2023. (a) Climatological 100-hPa geopotential height illustrating the SAH as an upper-tropospheric circulation system. The 16,720-gpm characteristic contour (orange-red) defines its areal extent (light shading) and southern, northern, western and eastern boundaries (arrows); the dot marks the climatological centre. The SAH intensity index is defined as the area-mean geopotential height over 20–35°N, 40–100°E (Section 2.3). (b) The WTV as a circulation variability mode, represented by the leading EOF of detrended JJA 200-hPa horizontal winds over 22–50°N, 50–92°E (40.1% of total variance; Wang et al., 2023). Shading and vectors show correlations of the standardized PC1 with 500-hPa geopotential height and horizontal wind, respectively; only correlations significant at $p < 0.05$ are shown. (c) Corresponding circulation pattern associated with the standardized Karakoram Zonal Index (KZI). The northern (U_N) and southern (U_S) KZI boxes are outlined; with U_S highlighted to indicate its latitudinal overlap with the southern flank of the SAH. The KZI associated pattern closely resembles the EOF1 pattern, with spatial correlation of 0.90 within the EOF domain and 0.80 over the displayed domain; the KZI and PC1 are correlated at R=0.78. The 1500-m orographic contour outlines the Tibetan Plateau.

Their seasonal behaviour provides a second distinction. The characteristic 100-hPa 16,720-gpm SAH contour is confined almost entirely to June-September: across 1979-2023, it occurs only once in May and is absent in winter (Figure 2a, b). By contrast, WTV variability occurs throughout the year and is strongest in winter and weakest in late summer (Li et al., 2018). The associated circulation anomaly has a deep, quasi-barotropic structure extending through much of the troposphere (Figure S1; Li et al., 2018, 2022). The two features therefore differ both in their definition and in their seasonal expression. The SAH is a strongly season-dependent circulation system, while the WTV represents a persistent, year-round mode of circulation variability. These differences show that the WTV cannot be identified simply with the occurrence or seasonal cycle of the SAH.

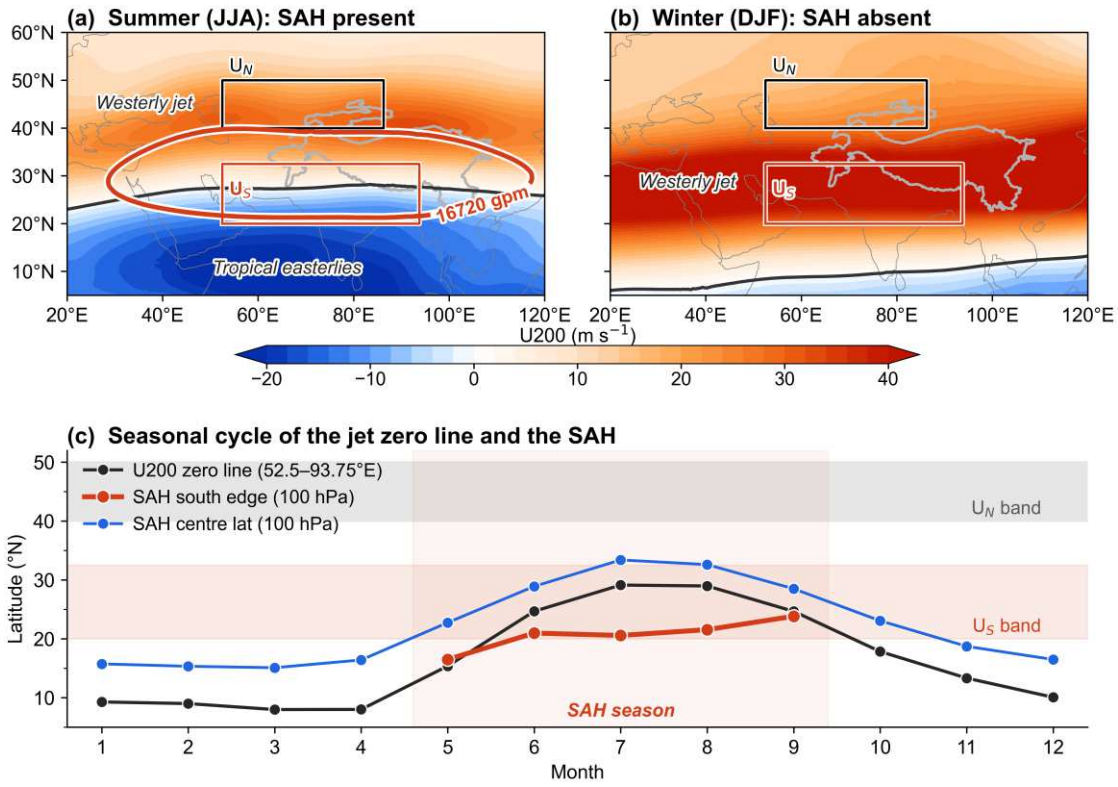


Figure 2. Seasonal contrast and summer overlap between the Western Tibetan Vortex (WTV) and South Asian High (SAH) during 1979–2023. (a, b) Climatological 200-hPa zonal wind (shading, zero-wind line contoured) and 100-hPa geopotential height in (a) summer (JJA) and (b) winter (DJF). The 16,720-gpm SAH characteristic contour (orange-red) is present in summer but absent in winter. The northern (U_N) and southern (U_S) KZI boxes are outlined; U_S is highlighted to show its latitudinal overlap with the easterly flow along the southern flank of the summer SAH . (c) Seasonal cycle of the 200-hPa zero-wind line latitude averaged over 52.5–93.75°E, together with the southern boundary and centre latitude of the 100-hPa SAH. Shading indicates the latitudinal ranges of the KZI boxes and the May–September period in which the 16,720-gpm contour occurs in the 1979–2023 climatology. The 1500-m orographic contour outlines the Tibetan Plateau.

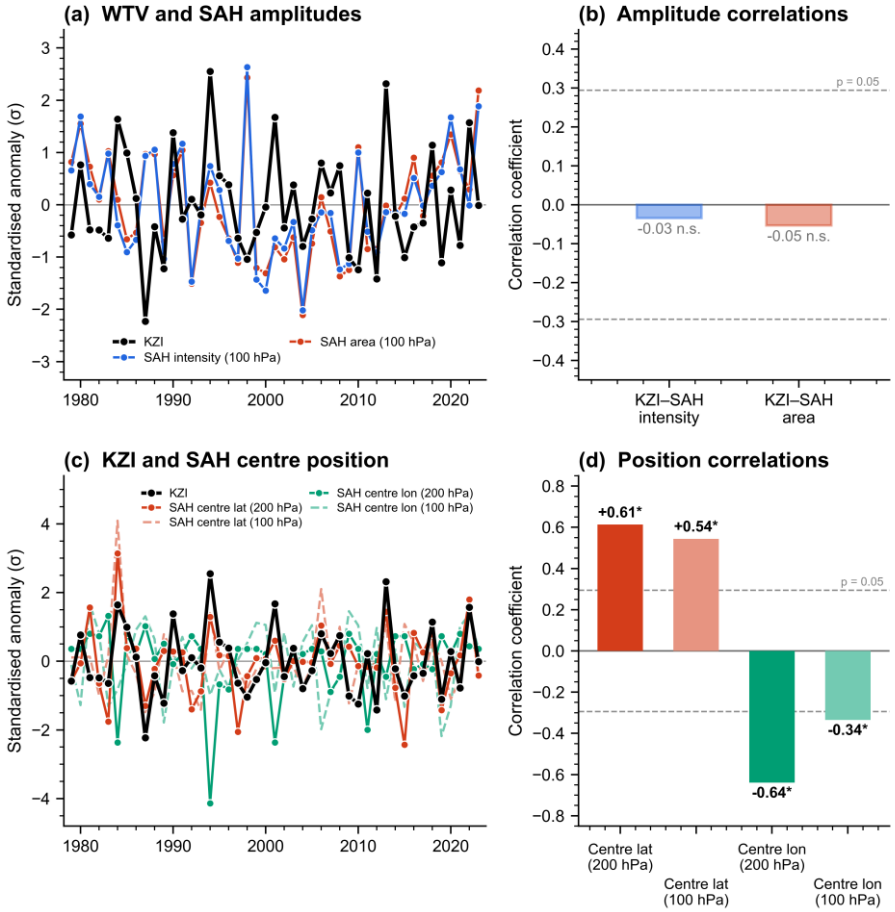


Figure 3. Selective relationship of summer WTV variability and SAH properties during 1979–2023. (a) Detrended standardised JJA time series of the KZI (black), 100-hPa SAH intensity (blue) and SAH area enclosed by the 16,720-gpm contour (vermillion). (b) Pairwise detrended correlations of the KZI with SAH intensity and area; neither relationship is statistically significant (both $p > 0.7$). (c) Detrended standardised JJA time series of the KZI (black) and the SAH centre latitude (vermillion) and centre longitude (teal) at 200 (solid) and 100 hPa (dashed). (d) Pairwise detrended correlations of the KZI with the SAH centre latitude and longitude at 200 and 100 hPa; all four relationships are significant at $p < 0.05$. The corresponding monthly relationships are shown in Figure S2.

3.2. Summer coexistence and structural overlap

Despite these distinctions, the WTV and SAH coexist in summer, when the fixed KZI domain partially overlaps the SAH circulation. In summer, the southern KZI box (U_s; 20–32.5°N) overlaps the easterly flow along the southern flank of the SAH (Figure 2a). The 1979–2023 JJA-mean zonal wind averaged over the U_S box is −2.7 m s^{-1}, and 61.0% of grid points within the box are climatologically easterly. In winter, by contrast, the same box is dominated by strong westerlies (43.6 m s^{-1}; Figure 2b). From June to September, the 200-hPa zero-wind line lies within U_S at 24.5–29°N (Figure 2c). This overlap raises the possibility that summer KZI variability contains a component associated with changes in the southern flank of the SAH.

Despite this structural overlap, summer WTV variability shows no significant relationship with either SAH intensity or areal extent. The KZI is not significantly correlated with either the intensity or areal extent of the 100-hPa SAH (R = −0.03 and −0.05, respectively, both p > 0.7; Figure 3a,b). This result indicates that interannual WTV variability cannot be explained simply by year-to-year changes in the SAH strength or size. By contrast, the SAH centre coordinates covary substantially with the KZI (Figure 3c,d), suggesting that the relationship is selective to SAH position. Section 4 tests this selectivity systematically across the full set of SAH diagnostics.

Table 1. Correlations of summer SAH characteristics with the KZI and its northern (U_N) and southern (U_S) zonal-wind components during 1979–2023.

SAH characteristic	r(KZI)	r(U_N)	r(U_S)
SAH amplitude			
Intensity (100-hPa area-mean HGT)	−0.03	+0.10	−0.00
Area enclosed by 16,720-gpm contour	−0.05	+0.02	−0.03
SAH centre position			
Centre latitude (200-hPa)	**+0.61*** **	+0.32*	−0.81***
Centre latitude (100-hPa)	**+0.54*** **	+0.28	−0.58***
Centre longitude (200-hPa_	**−0.64*** **	−0.54***	+0.51***
Centre longitude (100-hPa)	−0.34*	−0.36*	+0.07
SAH boundaries			
Southern boundary latitude	+0.28	+0.02	−0.35*
Northern boundary latitude	+0.21	+0.10	−0.31*
Western boundary longitude	−0.07	−0.06	+0.27
Eastern boundary longitude	−0.13	−0.04	+0.08

Note: Asterisks indicate unadjusted two-sided significance (* p < 0.05, ** p < 0.01, *** p < 0.001); boldface in the r(KZI) column indicates correlations that remain significant after the Benjamini–Hochberg false-discovery-rate correction at q = 0.05 (Section 2.1) All the time series are detrended before computing their correlations.

4. Selective coupling of WTV variability to SAH position

Section 3 showed that the WTV and SAH differ in their definition and seasonal expression, despite partial spatial overlap in summer. Because the southern KZI box partially overlaps the summer SAH circulation, however, covariance between the KZI and SAH diagnostics could arise partly from this geometrical overlap. We therefore examine which SAH characteristics are associated with WTV variability. The relationship is highly selective: the KZI is associated with SAH centre position (Figure 3c, d), but not significantly with its intensity, area, or boundary position (Table 1; Figure 3a, b; Figure 4a). Both the meridional and zonal centre displacements contribute to this relationship, with distinct signatures in the northern and southern KZI components.

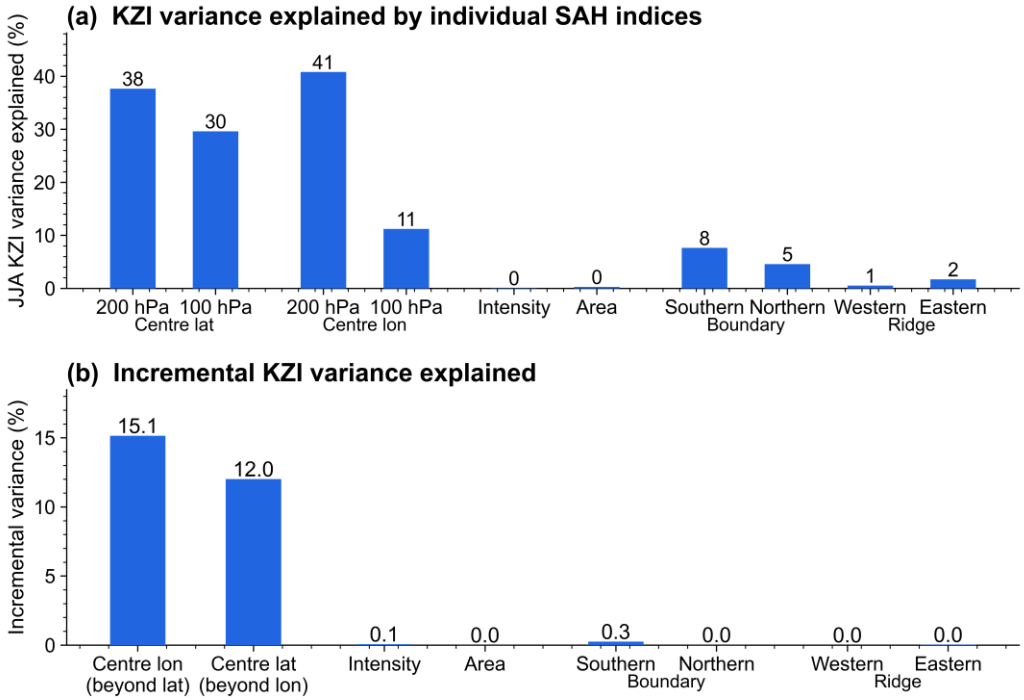


Figure 4. Selectivity of the relationship between summer WTV variability and SAH characteristics during 1979–2023. (a) Fraction of summer KZI variance explained by each SAH characteristic individually expressed as the coefficient of determination (R^2, %). (b) Joint and incremental variance explained by SAH centre position. Centre latitude and longitude together explain 52.8% of KZI variance. Centre longitude adds 15.1 percentage points of explained variance beyond centre latitude, whereas centre latitude adds 12.0 percentage points beyond centre longitude. Adding SAH intensity, area, or any individual boundary diagnostic to the two-coordinate centre-position model increases (R^2) by no more than 0.3 percentage points. All regressions are based on linearly detrended JJA time series.

SAH meridional position is strongly associated with WTV variability. SAH centre latitude is positively correlated with the KZI at both 200-hPa ($R = 0.61$, $p < 0.001$) and 100-hPa ($R = 0.54$, $p < 0.001$; Figure 3c,d), indicating that a northward-displaced SAH is associated with a more positive KZI. This relationship is dominated by the southern KZI component: centre latitude correlates with U_S at $R = -0.81$, compared with $R = 0.32$ for U_N. The stronger U_S relationship is consistent with the structural overlap identified in Section 3.2, because U_S samples the easterly flow along the southern flank of the SAH. By contrast, U_N lies outside the climatological SAH easterly belt in summer but remains significantly correlated with 200-hPa SAH centre latitude ($R = 0.32$; Table 1). The meridional relationship therefore cannot be attributed solely to the local overlap of U_S with the SAH flank. The relationship also persists when the KZI is recomputed at 500 hPa (Table S3), indicating that it is not confined to the 200-hPa index level.

SAH zonal displacement provides a second, comparatively strong, component of the relationship. At 200-hPa, SAH centre longitude is negatively correlated with the KZI ($R = -0.64$, $p < 0.001$) such that westward centre displacements

are associated with a more positive KZI (Table 1). Unlike the predominantly southern-component meridional relationship, the zonal relationship is evident in both KZI components, with opposite signs: R= −0.54 for U_N and R= 0.51 for U_S. This opposite-signed response is consistent with westward displacement of the SAH circulation producing stronger westerly anomalies to the north and easterly anomalies to the south over the KZI domain.

The meridional and zonal centre displacements provide partly distinct statistical contributions to KZI variability. SAH-centre latitude and longitude are moderately correlated (R = −0.49). Together, the two centre coordinates explain 52.8% of the summer KZI variance. Centre longitude adds 15.1% of explained variance beyond centre latitude, while centre latitude adds 12.0% explained variance beyond centre longitude (Figure 4b). By contrast, adding intensity, area, or any individual boundary diagnostic to the two-coordinate model increases R^2 by no more than 0.3 percentage points (Figure 4b). None of the four boundary diagnostics is significantly correlated with the KZI at the 5% level. The selectivity is also robust to multiple testing correction: among the 10 primary KZI–SAH correlations in Table 1, both centre-latitude relationships and the 200-hPa centre-longitude relationship remain significant after Benjamini–Hochberg false-discovery-rate correction at q = 0.05. Together, these results identify SAH centre position—rather than its overall intensity, areal extent, or contour boundaries—as the property most closely associated with summer WTV variability.

5. Pathways of SAH–WTV coupling: a jet-mediated route and a direct geometrical route

Section 4 showed that summer WTV variability is selectively associated with SAH position, rather than its intensity or areal extent. We next examine the circulation pathways consistent with this positional coupling. The diagnostics indicate two complementary routes (Figure 5a): a jet-mediated route, in which meridional SAH displacement is associated with jet position and, in turn, WTV variability, and a more direct geometrical route in which zonal SAH displacement projects its circulation onto the KZI definition boxes. We examine the SAH–jet and jet–WTV links in Sections 5.1 and 5.2, respectively, followed by the direct geometrical route in Section 5.3.

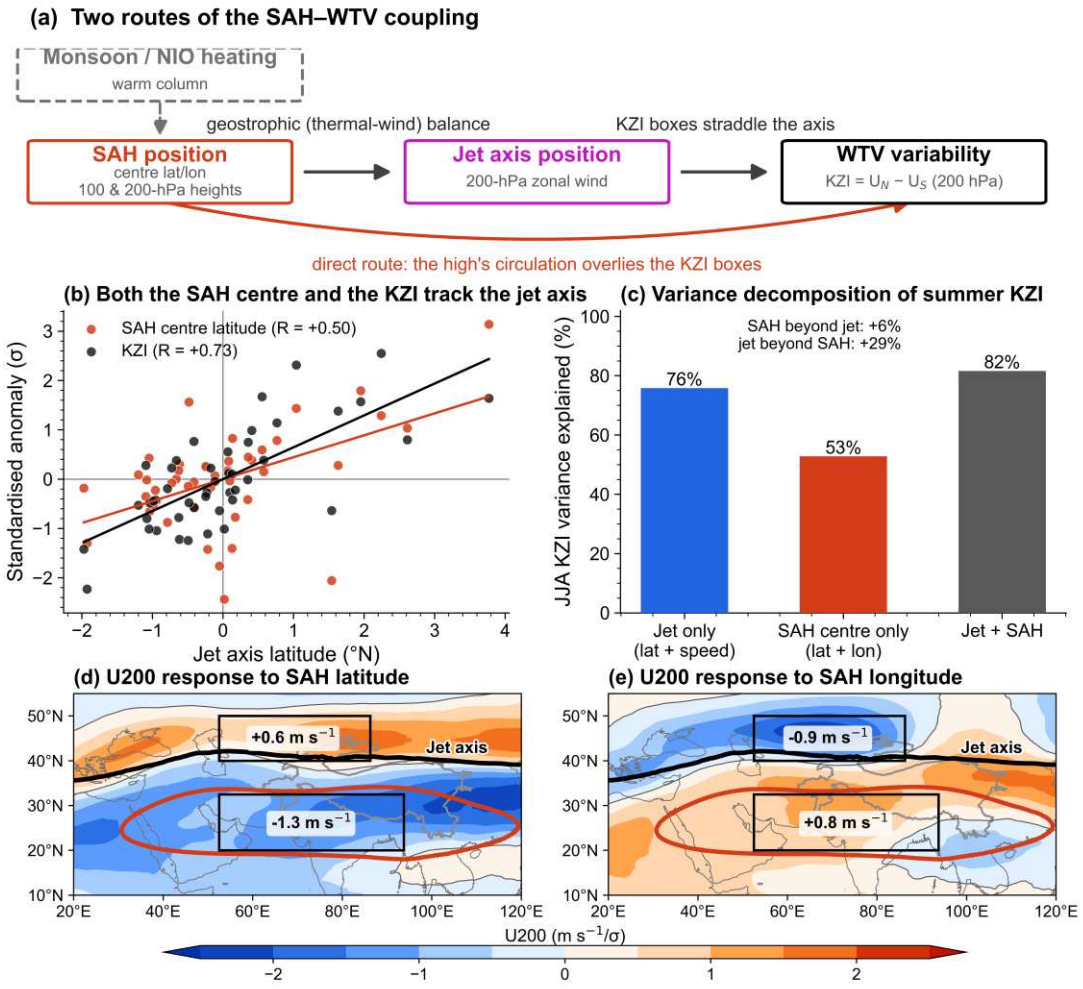


Figure 5. Statistical and circulation signatures of the two proposed routes of summer SAH–WTV coupling during 1979–2023. (a) Schematic overview of the jet-mediated route associated with meridional SAH displacement and the direct geometrical route associated with zonal displacement. The dashed connection indicates the monsoon/NIO-related warm column forcing examined in Figure S3 and the vermillion arc denotes the direct route; arrows denote the relationships examined in Sections 5.1–5.3. (b) Relationships of detrended, standardised JJA KZI anomalies (black) and 200-hPa SAH centre latitude (vermillion) with jet-axis latitude; lines show least-squares fits. (c) Variance in the summer KZI explained by SAH centre position, jet-axis latitude and speed, and their combined regression, including the corresponding incremental (R^2) contributions. (d, e) Detrended JJA 200-hPa zonal-wind anomalies regressed onto standardised SAH centre latitude (d) and centre longitude (e), respectively (shading; m s−1 per standard deviation of the predictor). The KZI definition boxes (solid), climatological jet axis (bold black) and climatological 12,500-gpm geopotential-height contour (vermillion) are shown; values within the boxes give the corresponding box-mean regression slopes. The monthly relationships are given in Figure S2.

5.1. The SAH–jet link

Consistent with the thermal forcing of the SAH (Section 1), the climatological temperature section shows a deep warm anomaly beneath the anticyclone (Figure S3a). Interannually, the warm-column amplitude is strongly correlated with SAH intensity and southern boundary latitude (R = 0.96 and −0.95, respectively) but only weakly with SAH centre

position ($|R| \leq 0.23$). It is also correlated with NIO SST ($R = 0.62$), whereas its relationship with monsoon rainfall is positive but not statistically significant ($R = 0.25$, and $|R| \leq 0.28$ across six alternative rainfall domains; Figure S3b, c). This contrast is consistent with the weak-temperature-gradient framework, which links subtropical free-tropospheric temperature more strongly to tropical SST than to local convection (Sobel et al., 2001; Xie et al., 2009). The warm-column and pathway statistics are summarised in Table S2.

SAH meridional position covaries strongly with the position of the subtropical westerly jet. SAH centre latitude is positively correlated with jet-axis latitude at both 200 hPa ($R = 0.50$, $p < 0.001$) and 100 hPa ($R = 0.78$, $p < 0.001$). Jet-axis latitude is also correlated with the northern SAH boundary ($R = 0.50$) but not with the southern boundary ($R = 0.21$, non-significant). Neither SAH intensity nor area is significantly correlated with the jet diagnostics. These relationships identify meridional SAH position, rather than intensity or area, as the SAH characteristic most closely associated with jet position.

This SAH–jet relationship is dynamically consistent with geostrophic balance rather than being solely a statistical coincidence. In the summer-mean circulation, the SAH height field and subtropical jet can be viewed as complementary manifestations of a largely balanced upper-tropospheric state: the SAH in the height field corresponds to the monsoon warm column, and the subtropical jet is the balanced wind anchored to the maximum meridional height gradient on the northern flank of the SAH. To leading order, the upper-tropospheric flow is close to quasi-geostrophic balance, in which the Coriolis force balances the horizontal pressure-gradient force (Holton, 2004). On pressure surfaces the zonal component of this balance can be written as:

$$f u_g = -g \frac{\partial Z}{\partial y} \quad \text{or} \quad u_g = -\frac{g}{f}\frac{\partial Z}{\partial y} \tag{4}$$

where f is the Coriolis parameter and Z is geopotential height; the geostrophic zonal wind (u_g) is therefore proportional to the meridional height gradient ($\frac{\partial Z}{\partial y}$). The climatological jet overlies the maximum meridional height gradient on the northern flank of the SAH, and the corresponding geostrophic wind (u_g) computed from that gradient ($\frac{\partial Z}{\partial y}$) is nearly indistinguishable from the observed wind, in both its meridional profile and its peak latitude (Figure 6a,b). Interannually, the latitude of the maximum height gradient closely tracks jet-axis latitude ($R = 0.94$), while the corresponding geostrophic wind speed closely tracks observed jet speed ($R > 0.99$; Figure 6c, d).

The SAH–jet link is therefore consistent with a balance constraint: meridional (north-south) shifts of the SAH are accompanied by shifts of its flank height gradients and, under geostrophic balance, by a shift in the position of the

subtropical jet. Because the KZI boxes straddle the climatological jet in summer, meridional jet displacement is accompanied by opposite-signed zonal-wind anomalies across the two boxes, and hence by KZI variability (Figure 7a). The associated wind response is evident in the regression onto SAH centre latitude (Figure 5d): a one-standard-deviation northward SAH displacement is associated with a 0.6 m s^{-1} increase in northern-box westerlies and a 1.3 m s^{-1} strengthening of southern-box easterlies.

The WTV wind response exhibits strong component asymmetry. The southern-KZI-box zonal wind correlates strongly with the SAH centre latitude at −0.81 ($p < 0.001$), whereas the northern-KZI-box response is much weaker ($R = 0.31$, $p = 0.03$; Figure 8c; Table S2). This contrast indicates the jet-mediated route primarily modulates the easterlies in southern-KZI-box. The full structure of this coupling is summarised schematically in Figure 7.

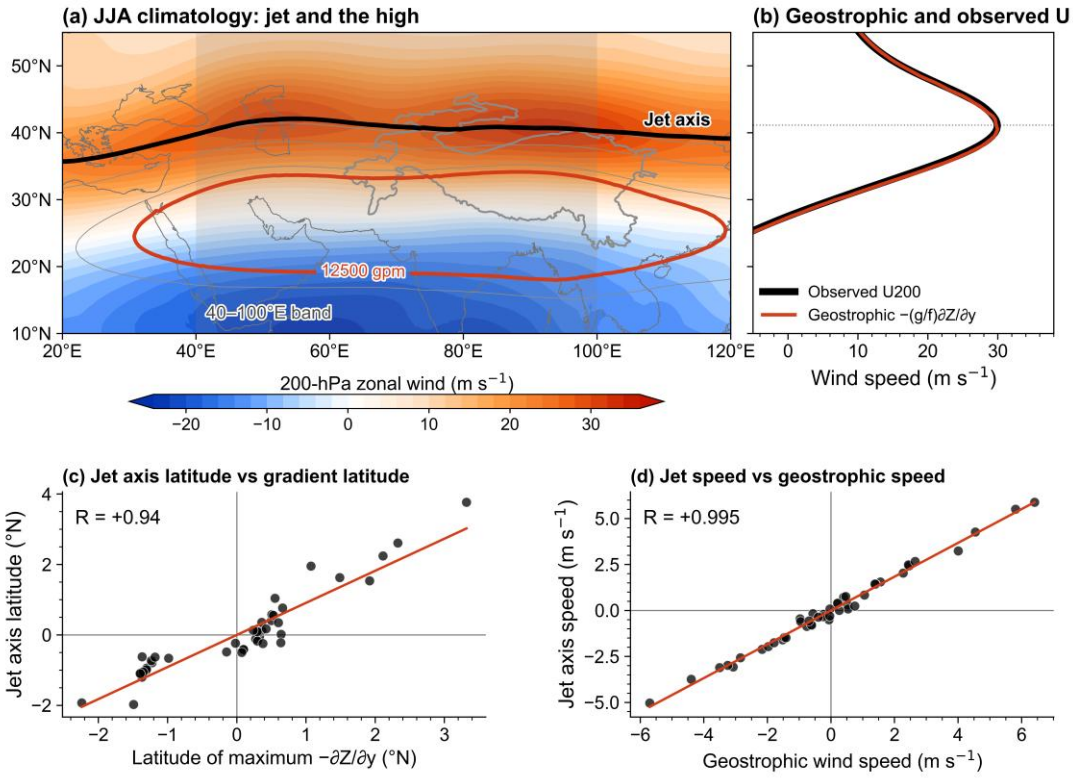


Figure 6. Geostrophic relationship between SAH height field and the subtropical westerly jet in summer during 1979–2023. (a) Climatological JJA 200-hPa zonal wind (shading) and geopotential height (grey contours; 12,500-gpm contour highlighted in bold vermillion). The shaded band indicates the 40–100°E averaging sector, and the bold black curve marks the climatological jet axis, defined as the latitude of maximum 200-hPa zonal wind at each longitude. (b) Climatological meridional profiles of 200-hPa zonal wind (black) and geostrophic zonal wind $-\frac{g}{f}\frac{\partial Z}{\partial y}$ calculated from the meridional geopotential-height gradient (vermillion), both zonally averaged over 40–100°E. The dotted line marks

the climatological jet-axis latitude. (c) Relationship between detrended JJA jet-axis latitude and the latitude of the maximum meridional geopotential-height gradient, calculated from the 40–100°E mean profiles. (d) Relationship between detrended jet-axis speed and the corresponding geostrophic wind speed. Lines in (c, d) show least-squares fits.

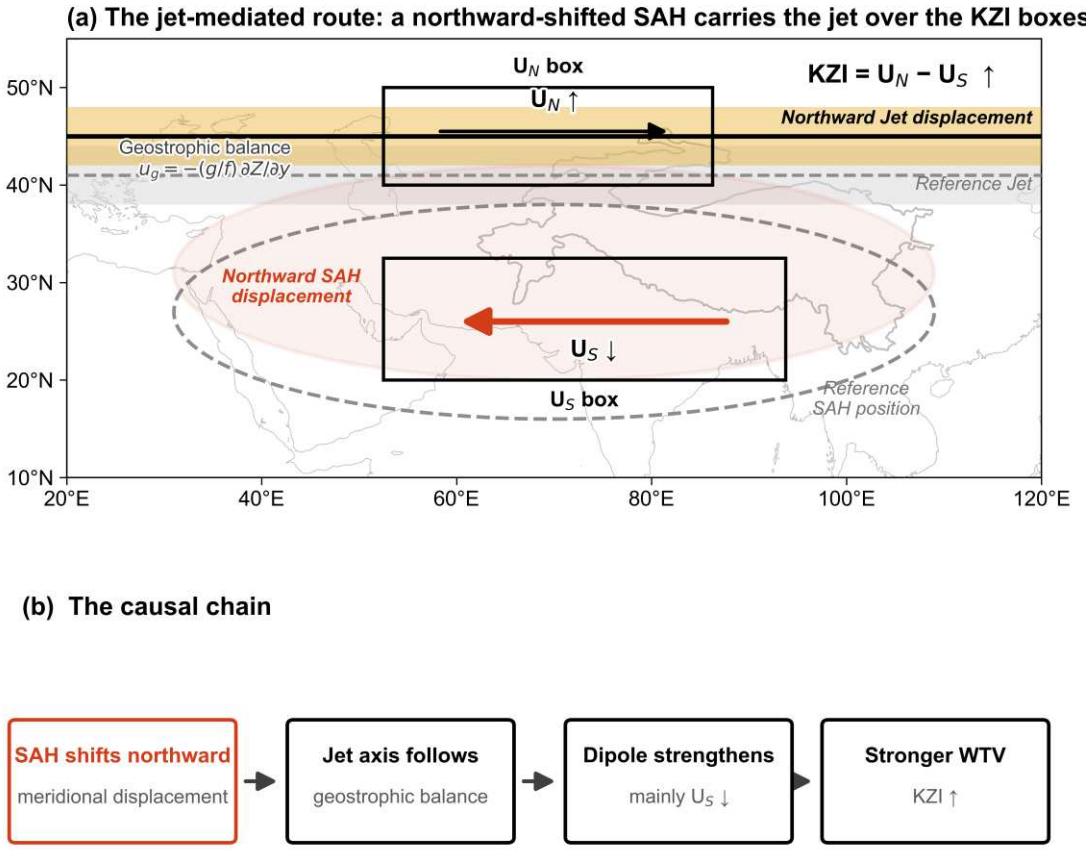


Figure 7. Schematic of the proposed jet-mediated route of summer SAH–WTV coupling. (a) Conceptual representation of the circulation changes associated with northward SAH displacement. The reference SAH position is shown by the dashed grey ellipse and the northward-displaced position by the vermillion ellipse. The associated northward displacement of the SAH northern-flank height gradient is accompanied by a northward shift of the subtropical westerly jet, consistent with geostrophic balance (reference jet in grey; displaced jet indicated by the bold black axis and orange band). The fixed KZI definition boxes (solid black) straddle the jet, such that the northward jet displacement is associated with stronger westerly flow in the northern box (U_N) and stronger easterly flow in the southern box (U_S). (b) Summary of the statistical pathway linking SAH meridional position, jet-axis latitude, and KZI variability; the relationship is expressed primarily through the southern-box easterlies (Table S2).

5.2. The jet–WTV link

The statistical relationships identify the subtropical westerly jet as an important intermediary between SAH meridional position and summer WTV variability. Jet-axis latitude and speed together explain 75.8% of summer KZI variance, compared with 52.8% explained by SAH centre position. Combining the SAH-position and jet predictors increases R^2 to 81.6% (Figure 5c; Table S2). Thus, the two predictor sets contain overlapping but partly distinct statistical information. Leave-one-out cross-validation, in which each summer is held out in turn and predicted from the remaining 44, yields explained variance of 46.0%, 71.9% and 74.6% for the SAH-position, jet and combined regressions, respectively, indicating that this explanatory power is not solely an in-sample property.

Incremental variance partitioning further distinguishes the information contained in the two predictor sets. After accounting for jet variability, adding SAH position increases R^2 by 5.8%. Conversely, adding the jet predictors to the SAH-position model increases R^2 by 28.8%. The partial correlations show a similar asymmetry: the KZI-jet–axis relationship remains strong ($R = 0.56$) after controlling for SAH position, whereas the KZI-SAH–centre-latitude correlation weakens substantially from 0.61 to 0.42 after controlling for jet variability.

A mediation-style analysis provides additional statistical evidence for a jet-mediated pathway. The estimated indirect effect through jet-axis latitude accounts for 46% (95% CI: 8–89%) of the SAH centre-latitude-KZI relationship and 42% (95% CI: 18–73%) of the NIO SST-KZI relationship (Figure 7b; Table S2). Because these diagnostics are based on contemporaneous seasonal-mean relationships, the mediation estimates describe a statistical pathway rather than establishing temporal causal direction. The associated circulation patterns are also consistent with this pathway: 200-hPa geopotential and wind anomalies associated with SAH centre latitude closely resemble those associated with jet-axis latitude. The two regression patterns have a spatial correlation of 0.74 within 20–50°N, 40–100°E (Figure 8a,b). Both SAH- and jet-associated patterns project onto the KZI domain, with the strongest relationship in the southern component (Figure 8c,d).

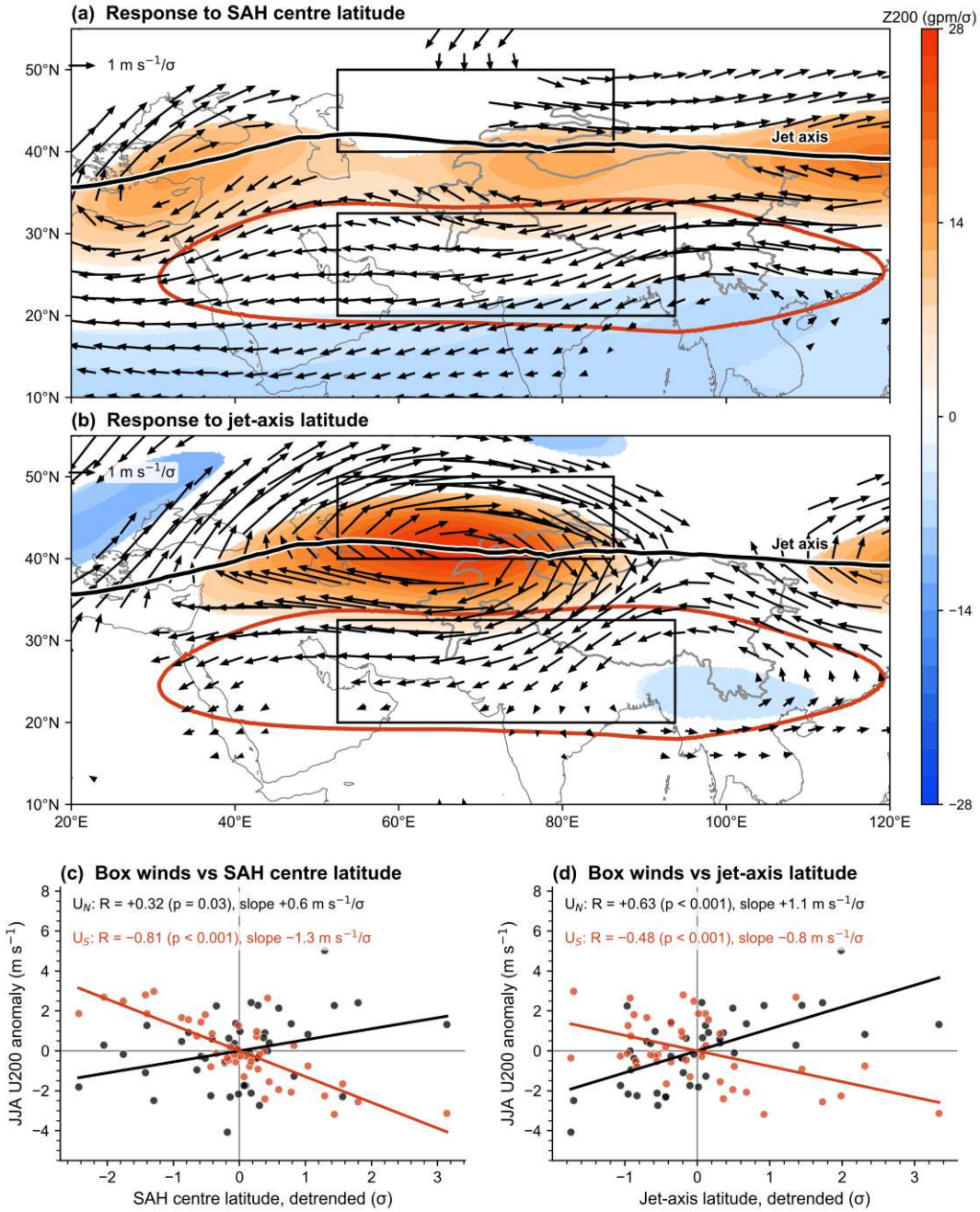


Figure 8. Circulation signatures of the jet-mediated SAH–WTV relationship in summer during 1979–2023. (a, b) Detrended JJA 200-hPa geopotential-height (shading, gpm per standard deviation of the predictor) and horizontal-wind (vectors, m s−1 per standard deviation) anomalies regressed onto standardised (a) SAH centre latitude and (b) jet-axis latitude. Shading and vectors are shown only where the corresponding regression is significant at ($p<0.05$). The climatological 12,500-gpm geopotential-height contour (vermillion), climatological jet axis (bold black) and KZI definition boxes (solid) are superimposed. (c, d) Relationships of detrended JJA 200-hPa zonal wind in the northern

436 (U_N, black) and southern (U_S, vermillion) KZI boxes with standardised (c) SAH centre latitude and (d) jet-axis latitude;
437 lines show least-squares fits.

438 The strength of this jet-mediated coupling exhibits pronounced seasonal dependence. The jet-latitude relationship
439 peaks in June (R = 0.85). The 100 hPa SAH-position relationships are strongest near monsoon onset and retreat, whereas
440 the 200-hPa coupling persists through mid-summer. The KZI-jet-speed coupling instead changes sign around May. In
441 winter, when the characteristic summer SAH structure is absent, WTV variability is associated primarily with jet
442 intensity rather than with the SAH diagnostics.

443

444 **5.3. The direct geometric route**

445 Unlike the jet-mediated meridional coupling, the zonal SAH–WTV relationship has a more direct geometrical
446 expression within the KZI domain. As summarised in Figure 9, westward SAH displacement is associated with an
447 anticyclonic circulation anomaly over the KZI domain, which simultaneously strengthens westerly flow in the northern
448 box and easterly flow in the southern box (Figure 5e).

449 This direct dynamical relationship exhibits distinct vertical stratification across the upper troposphere. At 200-hPa,
450 SAH centre longitude is significantly correlated with both KZI components ($R = -0.54$ for U_N and 0.51 for U_S, both $p < 0.001$; Figure 10b,c; Table S2). At 100-hPa, only the northern component is significantly related to centre longitude
452 ($R = -0.37$, $p = 0.014$), whereas the southern relationship is weak and non-significant ($R = 0.07$; Table S2). The zonal-
453 displacement signature is therefore most complete at 200 hPa, the level that defines the KZI.

454 This 200-hPa regression pattern illustrates this geometry directly (Figure 10a). Positive centre-longitude anomalies,
455 corresponding to eastward SAH displacement, are associated with positive height anomalies along the southern-to-
456 eastern flanks of the high and a compact negative height anomaly over the western Tibetan Plateau. This west–east
457 height-anomaly pattern reverses for westward displacement. The corresponding cyclonic wind anomaly for eastward
458 displacement lies between the KZI boxes, producing easterly anomalies in U_N and westerly anomalies in Us; the signs
459 reverse for westward displacement (Figure 10a,b,c). The regression slopes quantify the modulation: a one-standard-
460 deviation eastward displacement weakens the northern-box westerlies by 0.9 m s^{-1} and the southern-box easterlies by
461 0.8 m s^{-1}, with opposite-signed anomalies for a westward displacement. This north–south zonal-wind dipole is precisely
462 the configuration schematised for the direct route (Figure 9a,b). Thus, zonal SAH displacement projects directly onto

the opposite-signed winds used to define the KZI, consistent with geometrical superposition of the displaced SAH circulation onto the index.

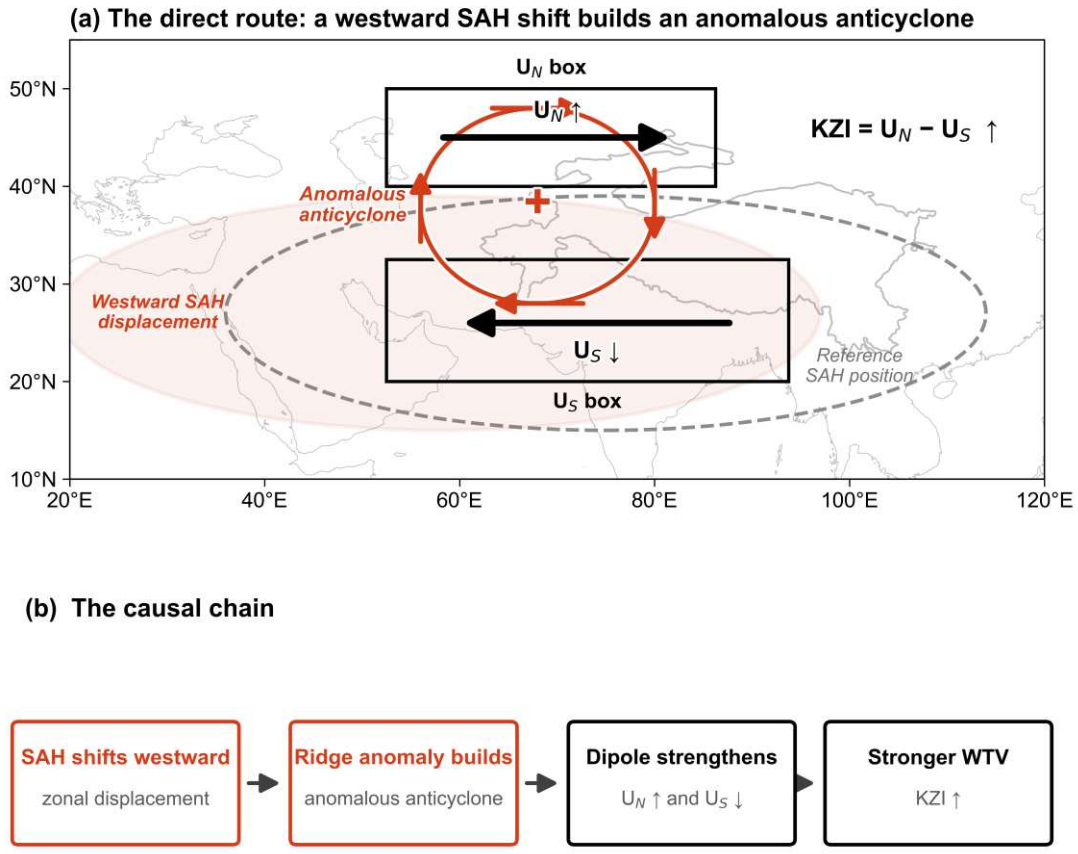


Figure 9. Schematic of the direct geometrical route of summer SAH–WTV coupling. (a) Conceptual representation of the circulation changes associated with westward SAH displacement. The reference SAH position is shown by the dashed grey outline and the westward-displaced position by the vermillion outline and shading. The displacement is associated with an anticyclonic circulation anomaly (vermillion gyre) over the western Tibetan Plateau between the fixed KZI definition boxes (solid black), producing stronger westerly flow in the northern box (U_N) and stronger easterlies in the southern box (U_S), consistent with the 200-hPa regression pattern in Figure 10a. (b) Summary of the statistical pathway linking SAH zonal displacement to KZI variability through its opposite-signed relationships with U_N and U_S at 200 hPa (Table S2).

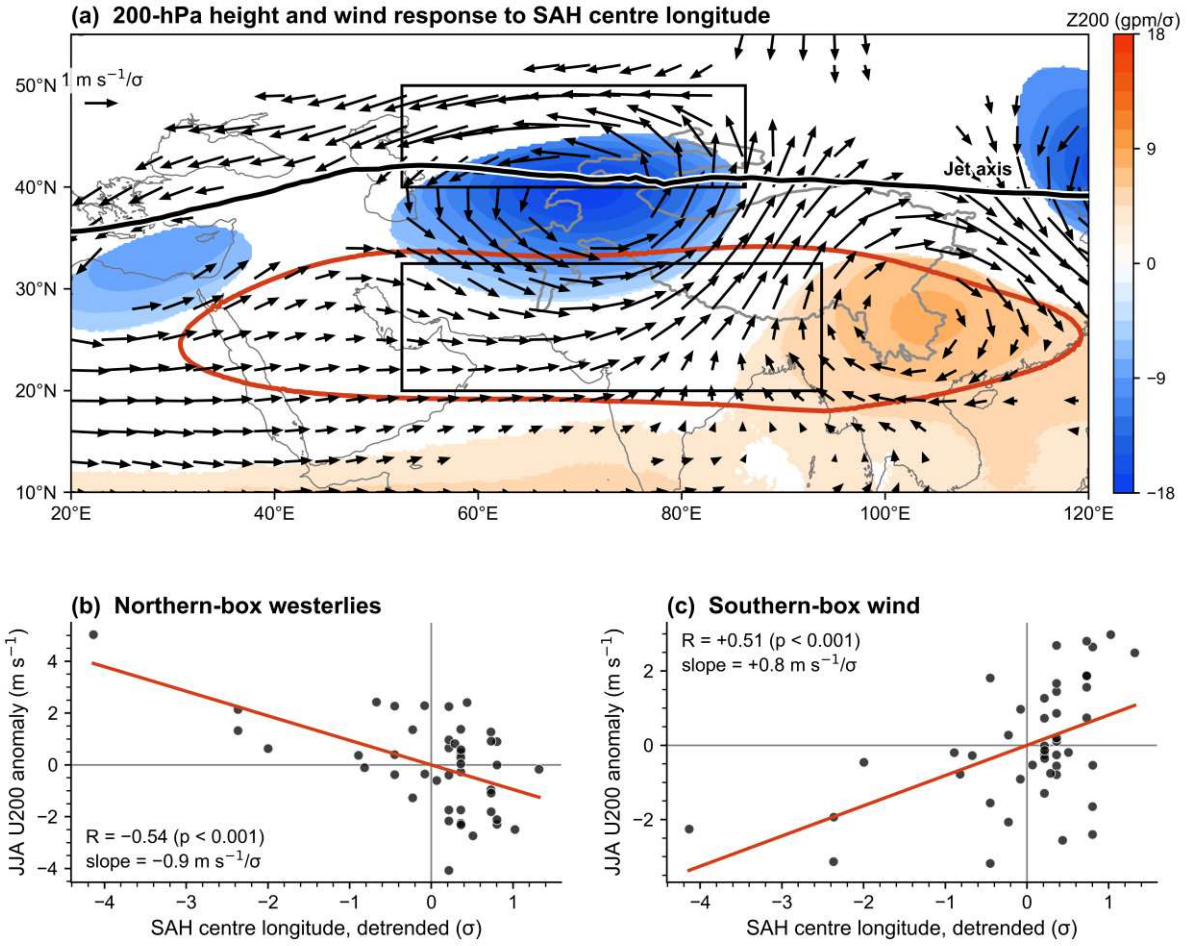


Figure 10. Circulation signatures of the direct geometrical SAH–WTV relationship in summer during 1979–2023. (a) Detrended JJA 200-hPa geopotential-height (shading, gpm per standard deviation of the predictor) and horizontal-wind (vectors, m s−1 per standard deviation) anomalies regressed onto standardised SAH centre longitude, with positive values denoting eastward displacement. Shading and vectors are shown only where the corresponding regression is significant at ($p<0.05$). The climatological 12,500-gpm geopotential-height contour (vermillion), climatological jet axis (bold black) and KZI definition boxes (solid) are superimposed. (b, c) Relationships of detrended JJA 200-hPa zonal wind in the (b) northern and (c) southern KZI boxes with standardised SAH centre longitude; lines show least-squares fits.

The two routes therefore provide complementary expressions of the observed SAH–WTV relationship. The jet-mediated meridional route is associated primarily with jet displacement and southern-box easterly variability (Figure 8c), whereas the direct zonal route projects onto both KZI boxes through displacement of the SAH circulation itself (Figure 10b,c). The latter is therefore consistent with geometrical superposition of the displaced SAH circulation onto the KZI-defining winds, rather than requiring transmission through the jet. The two routes are not statistically

independent, however, because SAH centre longitude also covaries with jet-axis latitude ($R = -0.48$ for the 200-hPa centre longitude; Table S2).

6. The western centre of the SAH and its relationship with the WTV

The preceding sections treated the SAH as a single circulation whose centre varies from year to year, consistent with its predominantly single-centred structure in summer-mean fields. At monthly to subseasonal timescales, however, a western centre over the Iranian Plateau has often been identified as either a preferred secondary centre or a distinct anticyclonic feature (Zhang et al., 2002; Qian et al., 2002; Liu et al., 2017; Zarrin et al., 2011; Tyrlis et al., 2013), and objective detection methods identify multiple coexisting centres more frequently in monthly and sub-daily fields (Peng et al., 2016; Siu and Bowman, 2020). The preferred-secondary-centre interpretation is closely related to the zonal oscillation of the SAH between its Iranian and Tibetan modes (Zhang et al., 2002), whose centre-longitude variability was shown in Sections 4 and 5.3 to be associated with the WTV. This raises a specific question: does the western centre at the levels relevant to the WTV represent the WTV itself, or is the relationship instead carried by continuous variability of the western flank of the SAH?

We distinguish the occurrence of a discrete western centre from continuous variability of the western ridge. The results show that the former is primarily a monthly-to-subseasonal feature and not associated with WTV variability, whereas the latter covaries closely with the WTV in summer-mean fields. We therefore first characterize the timescale dependence of the western centre (Section 6.1), then test its relationship with the WTV (Section 6.2), and finally examine how continuous western-ridge variability relates to the zonal-displacement relationship identified in Sections 4 and 5.3 (Sections 6.3-6.4).

6.1. The western centre is primarily a monthly-to-subseasonal feature

Using the 10-gpm prominence criterion defined in Section 2.3 to distinguish a separate maximum from a westward extension of the main high (Figure 11a,b), we find the summer-mean SAH is single-centred in all 45 summers at 100 and 150 hPa and in 44 of 45 summers at 200 hPa (Figure 11e,f). At monthly resolution, however, a distinct western centre occurs in 18 of 135 JJA 200-hPa fields, mostly in July (Figure 11c). In these cases , a local height minimum separates the western maximum from the main centre, as illustrated for July 1989 (Figure 11d). Thus, a discrete two-centre structure occurs intermittently at monthly timescales but is almost entirely absent from the summer mean.

The distinction between a western ridge and a discrete western centre is continuous rather than categorical in the underlying height field. The western ridge amplitude varies continuously, whereas a separate centre is identified only when a western maximum becomes sufficiently prominent to satisfy the 10-gpm criterion (Figure 11a, b).

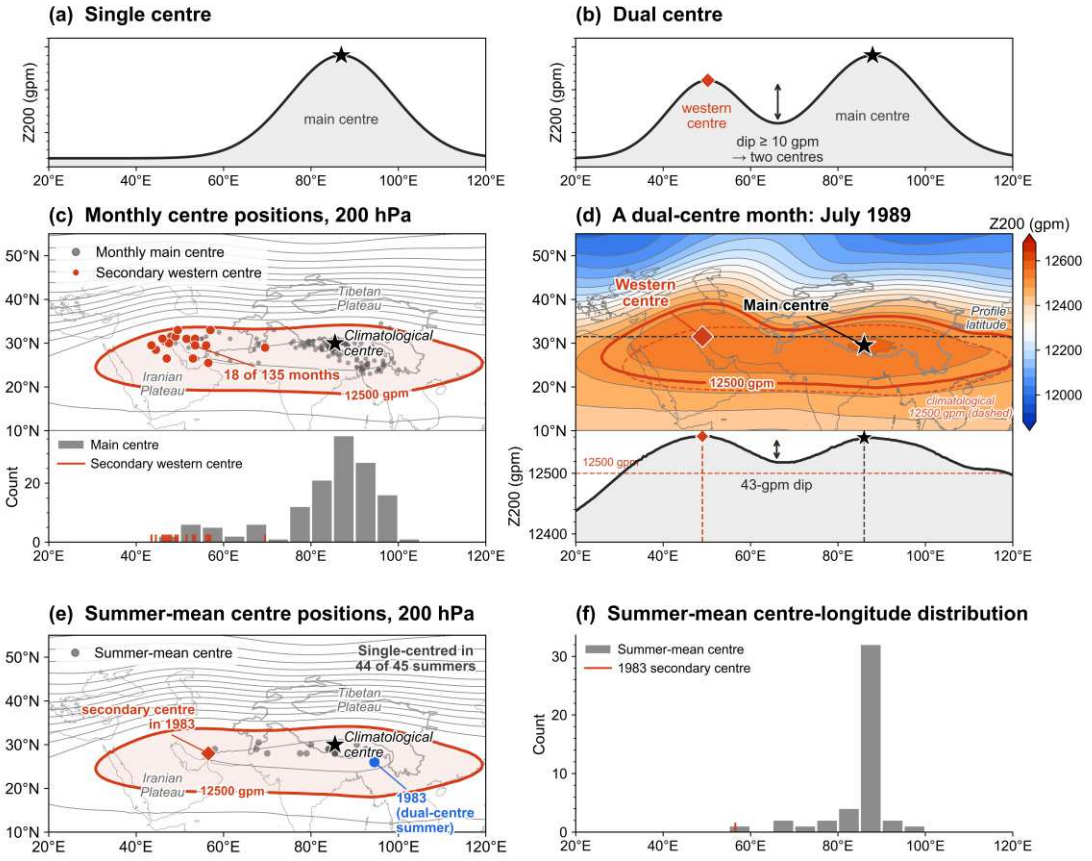


Figure 11. Timescale dependence of the western centre of the South Asian High (SAH) in summer during 1979–2023. (a, b) Schematic geopotential-height profiles along a latitude circle illustrating the centre-detection criterion: (a) a single-centred configuration and (b) a dual-centred configuration, in which a secondary western maximum is identified only when the intervening height lies at least 10 gpm below the adjacent maxima. (c) Locations of the main SAH centres (grey dots) and coexisting secondary western centres (vermillion dots) detected in 135 JJA monthly 200-hPa fields, superimposed on climatological JJA 200-hPa geopotential-height contours. The bold vermillion contour denotes 12,500 gpm, and the star marks the climatological SAH centre. The lower histogram shows the distribution of monthly main-centre longitude, with vermillion ticks indicating secondary-centre longitudes. (d) Example of a pronounced dual-centre configuration in July 1989, showing 200-hPa geopotential-height (shading), the main centre (star), and the secondary western centre (diamond). The solid and dashed vermillion contours denote the monthly and climatological 12,500-gpm contours, respectively. The lower panel shows the 200-hPa height profile along the latitude of the western centre, with a 43-gpm depression separating the two maxima. (e) SAH centre locations in 45 JJA-mean fields (grey dots). The circulation is single-centred in all 45 summers at 100 and 150 hPa and in 44 of 45 summers at 200 hPa; the exceptional year, 1983, is indicated by the blue dot (main centre) and vermillion diamond (secondary western centre). (f) Distribution of summer-mean SAH centre-longitudes, with the vermillion tick indicating the secondary centre detected in 1983.

This timescale dependence is consistent with the classical bimodality of the SAH. Using Sarle's bimodality coefficient (BC = (skewness² + 1)/kurtosis) for which BC > 5/9 indicates bimodality (Pfister et al., 2013), the monthly 100-hPa centre-longitude distribution is bimodal, with preferred positions near 55°E and 85°E (BC = 0.60), whereas the summer-mean distribution shows no clear bimodality (BC = 0.41). The preferred positions are also level-dependent. At 200 hPa, both preferred monthly main-centre longitudes lie over the Tibetan Plateau (80–100°E; Figure 11c), while a separate Iranian-Plateau maximum occurs only intermittently in the 18 dual-centre months. The detected frequency of multiple centres is sensitive to the prominence criterion, decreasing from 56% to 15% as the threshold increases from 2.5 to 20 gpm, which may partly explain the higher frequencies reported when less prominent secondary maxima are included (Peng et al., 2016). Overall, the discrete SAH western centre is primarily an intermittent monthly-to-subseasonal feature. In summer-mean fields, the separate western maximum is generally absent, and what remains of it is a westward extension of the main high toward the Iranian Plateau, a ridge whose strength varies from year to year.

6.2. The discrete western centre carries little WTV signal

The occurrence of a discrete western centre shows no detectable relationship with WTV amplitude. Among the 135 JJA monthly fields, a coexisting western centre is detected in 18 months, mostly in July, but KZI values do not differ significantly between months with and without such a centre ($t = -0.06$, $p = 0.95$; Figure S4a,b). Moreover, the circulation composite for dual-centre months does not resemble the KZI-associated regression pattern (pattern correlation −0.44; Figure S4d). Thus, the occurrence of a discrete western centre does not provide a useful indicator of WTV variability.

This null result does not reflect an absence of detectable WTV–SAH relationships at monthly resolution. Across the same 135 months, the west–east ridge-contrast correlates with the KZI at $R = 0.35$, 0.53, and 0.56 at 100, 150, and 200 hPa, respectively (all $p < 0.001$; Table S2), with the strongest monthly relationship occurring in June at 200 hPa ($R = 0.70$, $p < 0.001$; Figure S4c). All monthly significances are based on autocorrelation-corrected effective sample sizes (Section 2.1). The monthly record therefore contains a clear relationship between continuous western-ridge variability and the WTV, even though discrete splitting itself carries no detectable WTV signal.

6.3. Western-ridge amplitude covaries with the WTV

The continuous western-ridge amplitude shows a markedly different relationship with the WTV. As defined in Section 2.3, the west–east contrast index measures the height of the western flank relative to the eastern flank of the SAH, thereby reducing the contribution from basin-wide variations in the overall strength of the high.

In summer-mean fields, the west-east contrast correlates with the KZI at R = 0.38, 0.51, and 0.54 at 100, 150, and 200 hPa, respectively, strengthening with height (Figure 12a, b). By contrast, neither the maximum height on the western flank (R = 0.25, 0.23, and 0.19) nor the mean height over the broader western box (10–45°N, 20–70°E; R = −0.04, 0.14, and 0.18) is significantly correlated with the KZI (Figure 12b; Table S2). The relationship is therefore associated with the relative prominence and westward extension of the western ridge relative to the eastern high, rather than simply with the absolute height of the western SAH.

Western-ridge amplitude also contains statistical information beyond SAH centre-position. Adding the ridge-contrast index to the centre-position regression increases the explained KZI variance from 52.8% to 61.5% (Table S2). Consistently, the 200-hPa height-anomaly composite for strong-western-ridge summers closely resembles the KZI-associated regression pattern (pattern correlation = 0.81; Figure 12c). These results show that western-ridge variability at 150–200 hPa is closely associated with the WTV, although the two quantities are not identical.

The relationship also persists after removing the component of the KZI linearly associated with SAH meridional displacement. The resulting residual index KZI_{pure} retains 62% of the original KZI variance and correlates with the raw KZI at R = 0.79 (Figure S5a). Its associated circulation retains the characteristic WTV dipole structure, with spatial pattern correlations of 0.89 for wind and 0.85 for geopotential height relative to the raw-KZI patterns (Figure S5b–e; Table S2). Against this displacement-independent index, the west–east ridge contrast correlation remains correlated with KZI_{pure} at R = 0.54, 0.63, and 0.61 at the three levels (Figure 12b). Thus, the western-ridge relationship cannot be explained solely by the meridional-displacement component embedded in the summer KZI.

Western-ridge variability is nevertheless closely related to the zonal SAH displacement coupling documented in Sections 4 and 5.3. The KZI-centre-longitude relationship strengthens with height, from R = −0.35 at 100-hPa, to −0.48 at 150-hPa, and −0.64 at 200-hPa, while the ridge contrast correlates with the centre longitude at R = −0.56, −0.71, and −0.66 at the same levels (Figure 12b; Figure S6a). Removing the centre-longitude component reduces the 200-hPa ridge-contrast-KZI correlation to a non-significant 0.20. However, the ridge contrast still adds significant information beyond the full two-coordinate centre-position model (partial R = 0.43, p = 0.003; Figure S6b). The ridge contrast therefore provides a complementary western-flank measure of zonal SAH variability: it describes the height anomaly over the KZI domain more directly than does the coordinate of the SAH centre itself.

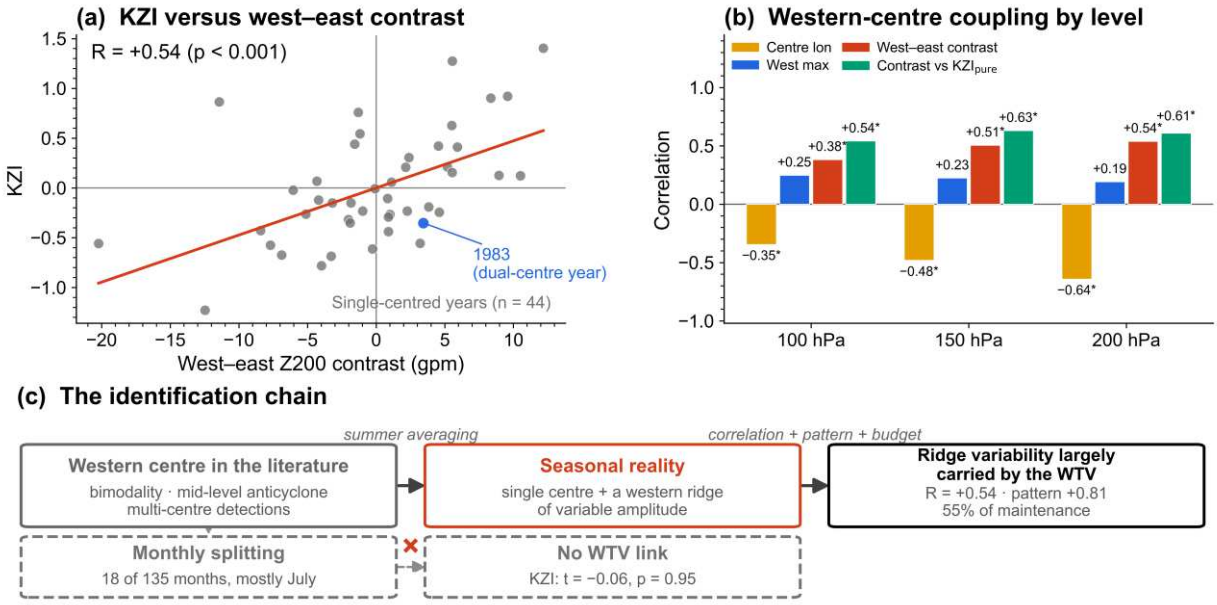


Figure 12. Relationship between summer WTV variability and the western ridge of the South Asian High (SAH) during 1979–2023. (a) Relationship between the detrended JJA west–east ridge-contrast index and the Karakoram Zonal Index (KZI). Grey dots represent summers with a single SAH centre, and the blue dot denotes 1983, the only summer with a distinct secondary western centre. The vermillion line shows the least-squares fit. (b) Correlations of the KZI with SAH centre longitude, western maximum geopotential height, and west–east ridge contrast at 100, 150, and 200 hPa, together with correlations of the ridge contrast with KZI_{pure}, defined as the KZI residual after removing its linear association with SAH centre latitude. Asterisks indicate statistical significance at $p < 0.05$. (c) Schematic synthesis of the relationships examined in Section 6, distinguishing the intermittent occurrence of a discrete western centre from continuous western-ridge variability and its association with the WTV and zonal SAH displacement.

6.4. Vorticity-budget characteristics of the western-ridge anomaly

The summer-mean vorticity budget provides additional dynamical context for the relationship between western-ridge and WTV variability. Strong western-ridge summers are characterized by an anticyclonic vorticity anomaly over the Iranian flank, flanked by cyclonic anomalies to the west and east, at both 200 and 100 hPa (Figure S7a, c). At 200 hPa this composite closely resembles the KZI-associated vorticity pattern (pattern correlation = 0.84).

Projected onto the western-ridge anomaly (Figure S7d), the summer-mean MAINT projection is 5.4×10^{-6} s^{-1} at 200 hPa, supporting the ridge, whereas the PROP, STRETCH and VERT projections are −8.2, −9.6 and -0.2×10^{-6} s^{-1}, respectively. The STRETCH opposition is dominated by its planetary part and reaches -20.2×10^{-6} s^{-1} at 100 hPa. The

residual term R' also projects positively onto the ridge, with 12.6×10^{-6} s^{-1} at 200 hPa, a contribution larger than any of the explicitly resolved terms. The summer-mean budget therefore does not permit a complete attribution of ridge maintenance; the alignment statements above concern the explicitly resolved linear terms only. In the projection framework of Section 2.5, MAINT is therefore spatially aligned with the western-ridge anomaly, whereas the other diagnosed terms oppose it.

The component of MAINT reconstructed from the KZI-associated anomaly also projects positively onto the western-ridge anomaly (Figure S7b). Its projection is 3.0×10^{-6} s^{-1}, equivalent to 55% of the full MAINT projection at 200 hPa (61% at 100 hPa). Thus, the major part of the anomalous-wind contribution to the summer-mean vorticity budget is associated with the independently defined WTV circulation.

This budget does not, however, establish the direction of interaction between the WTV and western ridge. A western-ridge anomaly necessarily carries a dynamically balanced wind anomaly that could produce a similar MAINT pattern, while the summer-mean budget does not resolve the temporal tendency required to distinguish cause from response. The results therefore demonstrate dynamical consistency between the WTV-associated circulation (Li et al., 2018, 2022) and western-ridge anomaly, rather than a one-way causal influence. Resolving the direction of interaction would require a daily tendency budget.

Taken together, these results distinguish two meanings of the SAH "western centre." A discrete coexisting western centre at 200 hPa is intermittent, occurring in only 18 of 135 summer months (Figure 11c) and its occurrence carries no detectable WTV signal, with WTV amplitude statistically unchanged ($p = 0.95$). It is instead a separate, intermittent feature of the SAH, the monthly-scale expression of the classical bimodality of the high. In contrast, the continuous western-ridge amplitude covaries closely with the WTV, particularly at 150–200 hPa, and this relationship persists after removal of the meridional SAH-displacement component from the KZI ($R = 0.54$ at 200 hPa, and 0.63 against KZI_{pure} at 150 hPa). The ridge variability is also closely related to the zonal SAH displacement identified in Sections 4 and 5.3. The western-centre relationship with the WTV is therefore better understood in terms of continuous western-flank variability of the SAH than as correspondence between the WTV and intermittent centre splitting.

7. Evaluation of SAH–WTV coupling in CMIP6 models

We assess whether the selective SAH–WTV relationships identified in Sections 4–6 are reproduced by 53 CMIP6 historical simulations over 1979–2014. For each model, the KZI, SAH centre position, intensity and area, subtropical jet characteristics, and west–east ridge contrast are calculated using the observational definitions. Correlations and

regression diagnostics are evaluated from linearly detrended JJA time series and compared with ERA5 over the same period (Table 2; Figure 13). This evaluation focuses on the internal relationships among the SAH, subtropical jet, and WTV. The NIO-related forcing links are examined in the companion study (Li et al., 2026) and are included in the full seven-link evaluation in Figure S8.

The models broadly reproduce the observed selectivity of SAH–WTV coupling with respect to SAH position rather than intensity or area. The correlations of the KZI with SAH centre latitude and longitude have the observed signs in 96% of models. Their ensemble-mean correlations are 0.57 and −0.44, respectively, compared with 0.58 and −0.57 in ERA5 (Figure 13a; Table 2). In contrast, the observed correlations with SAH intensity and area are close to zero (−0.02 and 0.05, respectively). Consistent with this weak observed association, the corresponding relationships are statistically non-significant in 70% and 88% of models. Nevertheless, the ensemble-mean intensity correlation is weakly positive (0.21), indicating a modest model tendency toward an intensity–KZI relationship that is absent in ERA5. Thus, the distinction between positional and amplitude-related SAH characteristics is broadly reproduced, although not uniformly across individual models.

The jet-related relationships are also reproduced in sign, but their magnitudes are systematically weaker than observed. The correlations between SAH centre latitude and jet-axis latitude, and between jet-axis latitude and the KZI, have the observed positive signs in 98% of models (Figure 13b; Table 2). However, their ensemble-mean values are only 0.32 and 0.49, compared with 0.78 and 0.75 in ERA5, respectively. The particularly large underestimate of the SAH–jet correlation indicates that models reproduce the direction of the meridional coupling more consistently than its strength. This discrepancy is compatible with previously documented biases in subtropical jet variability (Harvey et al., 2020; Zhou et al., 2022), although the present analysis does not isolate the source of the bias.

Table 2. Observations and CMIP6-simulated relationships among the South Asian High (SAH), subtropical westerly jet, and Western Tibetan Vortex (WTV) in summer during 1979–2014.

Relationship	Observed (ERA5)	CMIP6 mean [P10–P90]	Model agreement
SAH position–WTV relationships			
KZI vs SAH centre latitude	+0.58***	+0.57*** [+0.25, +0.79]	96%
KZI vs SAH centre longitude	−0.57***	−0.44*** [−0.65, −0.10]	96%
SAH amplitude–WTV relationships			
KZI vs SAH intensity†	−0.02	+0.21*** [−0.06, +0.49]	70% n.s.
KZI vs SAH area†‡	+0.05	−0.02 [−0.29, +0.28]	88% n.s.
Jet-mediated relationships			

SAH centre vs jet-axis latitude	+0.78***	+0.32*** [+0.11, +0.54]	98%
KZI vs jet-axis latitude	+0.75***	+0.49*** [+0.18, +0.77]	98%

Note: For observational–model consistency the SAH centre is taken from the 100 hPa height field in both. P10–P90 is the 10th–90th percentile range across models. † For the two amplitude links the observed correlation is near zero; the last column instead gives the share of models with a non-significant (n.s.) correlation ($|R| < 0.33$, $p > 0.05$). ‡ Computable in 34 of the 53 models (the 16,720-gpm contour is absent or covers the domain in the remaining models). Asterisks on the observed values follow Table 1. Asterisks on the model means denote the cross-model significance of the ensemble-mean correlation (one-sample t-test on the Fisher-z-transformed correlations across the 53 models, following Wilks (2011); $p < 0.001$ for the five marked links; the area link is non-significant). All observed values are computed from ERA5.

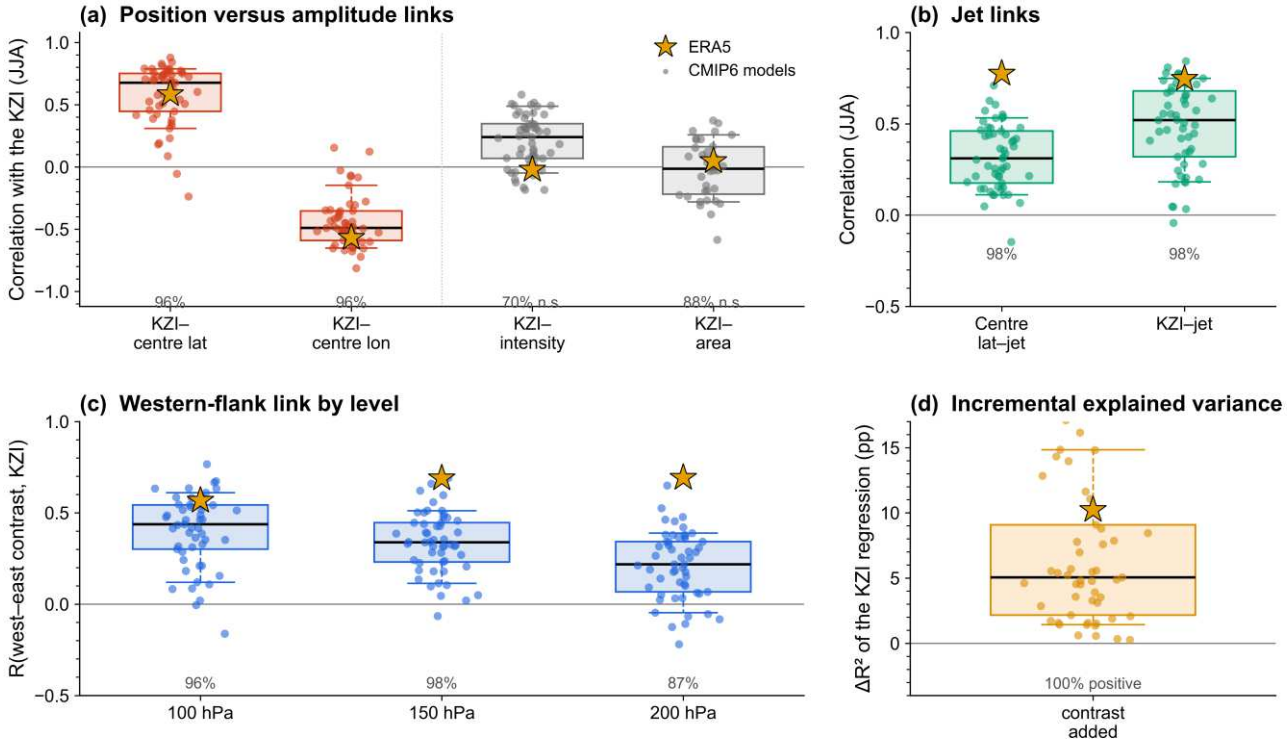


Figure 13. Evaluation of summer SAH–WTV coupling in 53 CMIP6 historical simulations during 1979–2014. (a) Cross-model distributions of correlations between the Karakoram Zonal Index (KZI) and SAH centre latitude, centre longitude, intensity and area at 100-hPa. (b) As in (a), but for correlations between SAH centre latitude and subtropical jet-axis latitude, and between jet-axis latitude and the KZI. (c) Cross-model distributions of correlations between the KZI and the west–east SAH ridge contrast index at 100, 150 and 200 hPa. (d) Cross-model distribution of the incremental explained variance obtained by adding the 200-hPa ridge contrast index to a multiple regression of the KZI on SAH centre latitude and longitude. All correlations and regressions are calculated from linearly detrended JJA time series. Boxes indicate the 25th–75th percentiles, dashed whiskers the 10th–90th percentiles, and dots individual models; stars denote the corresponding ERA5 values over 1979–2014. Annotations indicate the percentage of models reproducing the observed correlation sign, except for the SAH-intensity and SAH-area relationships, for which they indicate the percentage of models with statistically non-significant correlations ($p > 0.05$). SAH area is available in 34 models; all other diagnostics use 53 models. The extended evaluation, including NIO-related forcing links, is presented in Figure S8.

A further cross-model test supports the relevance of the jet-mediated relationship. Models with stronger SAH–jet correlations also tend to exhibit stronger jet–KZI correlations (cross-model R = 0.38, p = 0.006; Figure S8c). The analogous cross-model relationships for the SAH–KZI and NIO–KZI link pairs are weaker and not statistically significant (R = 0.21 and 0.19, respectively; Figure S8b,d). This contrast provides additional evidence that the SAH–jet and jet–WTV relationships form a coherent statistical pathway across the model ensemble. It does not, however, establish the temporal or causal direction of the coupling.

The models also reproduce the association between western-ridge variability and the WTV identified in Section 6. The west–east ridge contrast correlates positively with the KZI at 100, 150 and 200 hPa in 87–98% of models (Figure 13c). The corresponding ensemble-mean correlations are 0.40, 0.34 and 0.21, compared with 0.57, 0.69 and 0.69 in ERA5 over 1979–2014. The pronounced weakening of the simulated relationship at 150–200 hPa indicates that models capture its vertical occurrence and sign more successfully than its observed strength.

The western-ridge contrast also provides additional explanatory information beyond SAH centre position. Adding the 200-hPa ridge contrast to a regression containing SAH centre-latitude and longitude increases the explained summer KZI variance in every model. The mean increment is 7.1 percentage points, compared with 10.2 percentage points in ERA5 (Figure 13d). Because an additional predictor cannot reduce ordinary least-squares (R^2), this universally positive increment should be interpreted primarily in terms of its magnitude rather than its occurrence. The model-mean increment nevertheless indicates that western-ridge variability contains information about the KZI not fully represented by the SAH centre coordinates.

Overall, the 53 CMIP6 models reproduce three central features of the observed summer SAH–WTV relationship: the predominance of SAH position over intensity and area, the positive relationships connecting SAH meridional position, jet latitude, and WTV variability, and the association between western-ridge amplitude and the KZI. The consistency of these relationships across models supports their robustness beyond the ERA5 record. However, the models substantially underestimate the observed SAH–jet and upper-level western-ridge correlations. The ensemble therefore reproduces the principal statistical structure of the coupling more successfully than its quantitative strength.

8. Conclusions and discussion

This study clarifies the distinction and selective coupling between the Western Tibetan Vortex (WTV) and the South Asian High (SAH) using ERA5 reanalysis for 1979–2023 and historical simulations from 53 CMIP6 models. By combining circulation diagnostics, statistical decomposition, and vorticity-budget analysis, we distinguish the WTV as

a recurrent circulation-variability mode from the SAH as a summer anticyclonic circulation system, quantify their position-dependent relationships, and reassess the interpretation of the SAH's western centre. The principal findings are as follows.

(1) **The WTV and SAH are distinct atmospheric phenomena**. The SAH is a thermally driven, upper-tropospheric anticyclone that develops primarily in summer, whereas the WTV is a year-round circulation-variability mode with a deep, quasi-barotropic structure (Li et al., 2018, 2022). Although their circulation patterns overlap spatially during summer, WTV amplitude is not significantly related to SAH intensity or area. Their spatial coexistence therefore does not imply that the WTV is a component of the SAH.

(2) **Their summer variability is selectively coupled through SAH position rather than strength**. SAH centre latitude and longitude jointly explain 53% of the interannual variance in the summer Karakoram Zonal Index (KZI). Two complementary statistical pathways characterize this relationship. Meridional (north-south) SAH displacement is associated with changes in subtropical jet latitude and speed, which together explain 76% of KZI variance. Zonal (east-west) SAH displacement is associated with anticyclonic circulation anomalies over the western Tibetan Plateau that project directly onto the KZI wind components. These jet-mediated and direct geometrical relationships provide a coherent description of the observed coupling, although their causal direction cannot be established from contemporaneous regressions alone.

(3) **The SAH western-ridge relationship with the WTV differs fundamentally from the occurrence of a discrete western centre.** At 200 hPa, a distinct secondary western centre occurs in only 18 of 135 summer months and shows no detectable association with KZI amplitude. In contrast, continuous western-ridge variability at 150–200 hPa covaries closely with the WTV and is related to zonal SAH displacement. Removing the component of the KZI linearly associated with SAH meridional displacement leaves 62% of its original variance and preserves the characteristic WTV circulation pattern. The summer-mean vorticity budget further demonstrates dynamical consistency between WTV-associated winds and western-ridge anomalies, without resolving the direction of their interaction.

(4) **CMIP6 models broadly reproduce the coupling structure but underestimate several observed relationships**. Most of the 53 models reproduce the observed signs of the SAH-position and jet-related correlations, as well as the positive western-ridge–KZI relationship. Across models stronger SAH–jet coupling is associated with stronger jet–WTV coupling. Nevertheless, the ensemble substantially underestimates the observed SAH–jet and upper-level

western-ridge correlations. Thus, the models reproduce the qualitative structure and selectivity of the coupling more successfully than its quantitative strength.

These findings resolve an important conceptual ambiguity. The SAH is a circulation system identified from the atmospheric height and wind fields, whereas the WTV describes a recurrent mode of circulation variability over the western Tibetan Plateau. A variability mode may overlap a circulation system and covary with its displacement without constituting a distinct component of that system. The persistence of the WTV outside summer, its weak relationship with SAH intensity and area, and the retention of its characteristic circulation after removing the meridional SAH-displacement component all support this distinction. The WTV is therefore neither a separate summer anticyclone nor simply the western centre of the SAH; it is a circulation-variability mode whose summer expression is selectively associated with SAH position.

The results also connect two previously distinct lines of research. Studies of the SAH have emphasized its meridional displacement and zonal oscillation between Tibetan and Iranian modes (Zhang and Wu, 2001; Zhang et al., 2002), whereas studies of the WTV have highlighted its year-round variability and seasonal relationship with the subtropical jet (Li et al., 2018, 2022). Our analysis quantitatively links these perspectives through the SAH's positional variability. In particular, the association between KZI and continuous SAH centre longitude does not require a bimodal distribution of centre positions, an issue that remains debated (Nützel et al., 2016). The jet-mediated relationship also helps explain why SAH–WTV coupling is most prominent during summer (Li et al. 2018), when the upper-tropospheric anticyclone and subtropical jet exhibit strong meridional covariability.

The interpretation of the SAH western centre requires particular attention to vertical level and temporal averaging. Previous studies have described the western centre in terms of Iranian Plateau heating, regional subsidence and heating over the Zagros Mountains, or intermittent splitting of the monsoon anticyclone (Zhang et al., 2002; Qian et al., 2002; Liu et al., 2017; He et al., 2019; Zarrin et al., 2011; Tyrlis et al., 2013; Siu and Bowman, 2020). These interpretations need not be mutually exclusive because they concern different aspects of the circulation. Our results show that discrete centre splitting is primarily a monthly-to-subseasonal feature, whereas the continuous western ridge in summer-mean fields at 150–200 hPa is closely associated with WTV variability. This distinction is compatible with the height-dependent structure and westward tilt of the SAH (Jia and Liu, 2020), but does not establish that the WTV dynamically maintains the western ridge.

Several limitations point to future research priorities. First, the observed relationships are based mainly on simultaneous seasonal statistics. Although the jet-mediated and direct geometrical pathways are consistent with the circulation structure and geostrophic balance, their temporal ordering and possible feedbacks remain unresolved. The summer-mean vorticity budget likewise identifies terms aligned with western-ridge anomalies but lacks the tendency information needed to determine whether WTV-associated circulation changes precede or follow ridge development. Daily or subseasonal tendency budgets, together with targeted numerical experiments, would help distinguish these possibilities.

Second, the role of external forcing warrants further investigation. Tropical-thermal influences associated with the northern Indian Ocean and Indian Ocean Basin Mode may affect the SAH and subtropical jet (Yang et al., 2007; Xie et al., 2009; Huang et al., 2011), while disturbances associated with Rossby wave propagation, including those linked to the North Atlantic Oscillation, may influence the WTV more directly (Lei et al., 2025). Potential influences of ENSO on autumn WTV variability also merit examination (Jiang et al., 2025). How these forcing pathways interact, and whether they modify the strength or direction of SAH–WTV coupling, remains an open question. Finally, the pronounced seasonal dependence of the relationships (Figure S2), together with the systematic underestimation of their strength in CMIP6 models, suggests opportunities to investigate seasonally dependent WTV predictability and the model processes controlling its representation.

Overall, the WTV and SAH should be regarded as distinct but selectively coupled aspects of the upper-tropospheric circulation. Their summer relationship is organized primarily by SAH displacement, subtropical jet variability, and the continuous western ridge rather than by SAH intensity or intermittent centre splitting. This distinction provides a clearer framework for interpreting the dynamics, climate variability, and model representation of the circulation over the western Tibetan Plateau.

Acknowledgements:

This study is funded by the National Key R&D Program of China (2025YFF0812000), the National Natural Science Foundation of China (42175026; 42475036) and the Southern Marine Science and Engineering Guangdong Laboratory (Zhuhai) (SML2024SP012).

Author contributions:

X.-F.L. conceived the study, performed the analyses, and wrote and revised the manuscript. H.J.F. and S.Y. participated in the discussion of the results and revised the manuscript. S.Y. acquired the funding. B.L. and Y.L. performed part of the calculations. All authors read and approved the final manuscript.

Data availability:

The ERA5 monthly pressure-level fields are available from the Copernicus Climate Data Store (https://cds.climate.copernicus.eu). The ERSSTv6 data are provided by the NOAA Physical Sciences Laboratory (https://psl.noaa.gov/data/gridded/data.noaa.ersst.v6.html). The CMIP6 model output is openly available through the Earth System Grid Federation (https://esgf-node.llnl.gov/). The unified WTV–SAH index dataset and the analysis scripts are available from the corresponding author upon reasonable request.

Code availability:

The analysis scripts underlying the results and figures of this study are available from the corresponding author upon reasonable request.

Competing interests:

All authors declare no financial or non-financial competing interests.

References

Baron R M, Kenny D A. 1986. The moderator–mediator variable distinction in social psychological research: Conceptual, strategic, and statistical considerations. J Pers Soc Psychol, 51: 1173–1182

Bretherton C S, Widmann M, Dymnikov V P, et al. 1999. The effective number of spatial degrees of freedom of a time-varying field. J Clim, 12: 1990–2009

Ding Q, Wang B. 2005. Circumglobal teleconnection in the Northern Hemisphere summer. J Clim, 18: 3483–3505

Efron B. 1979. Bootstrap methods: Another look at the jackknife. Ann Stat, 7: 1–26

Eyring V, Bony S, Meehl G A, et al. 2016. Overview of the Coupled Model Intercomparison Project Phase 6 (CMIP6) experimental design and organization. Geosci Model Dev, 9: 1937–1958

Feldstein S B. 2002. Fundamental mechanisms of the growth and decay of the PNA teleconnection pattern. Q J R Meteorol Soc, 128: 775–796

Forsythe N, Fowler H J, Li X F, et al. 2017. Karakoram temperature and glacial melt driven by regional atmospheric circulation variability. Nat Clim Change, 7: 664–670

Harvey B J, Cook P, Shaffrey L C, et al. 2020. The response of the Northern Hemisphere storm tracks and jet streams to climate change in the CMIP3, CMIP5, and CMIP6 climate models. J Geophys Res-Atmos, 125: e2020JD032701

He B, Liu Y, Wu G, et al. 2019. The role of air–sea interactions in regulating the thermal effect of the Tibetan–Iranian Plateau on the Asian summer monsoon. Clim Dyn, 52: 4227–4245

Hersbach H, Bell B, Berrisford P, et al. 2020. The ERA5 global reanalysis. Q J R Meteorol Soc, 146: 1999–2049

Holton J R. 2004. An Introduction to Dynamic Meteorology. 4th ed. San Diego: Elsevier Academic Press

Hoskins B J, Rodwell M J. 1995. A model of the Asian summer monsoon. Part I: The global scale. J Atmos Sci, 52: 1329–1340

Huang B, Yin X, Boyer T, et al. 2025a. Extended reconstructed sea surface temperature, version 6 (ERSSTv6). Part I: An artificial neural network approach. J Clim, 38: 1105–1121

Huang B, Yin X, Boyer T, et al. 2025b. Extended reconstructed sea surface temperature, version 6 (ERSSTv6). Part II: Upgrades on quality control and large-scale filter. J Clim, 38: 1123–1136

Huang G, Qu X, Hu K. 2011. The impact of the tropical Indian Ocean on South Asian High in boreal summer. Adv Atmos Sci, 28: 421–432

Jia J Y, Liu Y. 2020. Spatial-temporal characteristics of the Asia High warm center and atmospheric waves excited by it in upper troposphere. Chinese J Geophys, 63: 3626–3639 (in Chinese)

Jiang Y, Li X F, Zhou X, et al. 2025. Impacts of ENSO on atmospheric circulation over the western Tibetan Plateau in autumn. J Clim, 38: 4251–4261

Kolstad E W, O'Reilly C H. 2024. Causal oceanic feedbacks onto the winter NAO. Clim Dyn, 62: 4223–4236

Krishnamurti T N, Daggupaty S M, Fein J, et al. 1973. Tibetan high and upper tropospheric tropical circulations during northern summer. Bull Am Meteorol Soc, 54: 1234–1250

Lei B B, Li X F, Li Y J, et al. 2025. Impacts of NAO on Western Tibetan Vortex: Summer versus winter features. J Trop Meteorol, 31: 565–574

Li X F, Fowler H J, Forsythe N, et al. 2018. The Karakoram/Western Tibetan vortex: seasonal and year-to-year variability. Clim Dyn, 51: 3883–3906

Li X F, Fowler H J, Yu J, et al. 2019. Thermodynamic controls of the western Tibetan vortex on Tibetan air temperature. Clim Dyn, 53: 4267–4290

Li X F, Yu J, Liu S, et al. 2022. Structure of the Western Tibetan Vortex inconsistent with a thermally-direct circulation. Clim Dyn, 58: 2213–2225

Li X F, Yu J, Li Y, et al. 2026. Spring ENSO predicts summer Western Tibetan Vortex intensity through an Indian Ocean relay. Submitted

Lin Z, Lu R. 2005. Interannual meridional displacement of the East Asian upper-tropospheric jet stream in summer. Adv Atmos Sci, 22: 199–211

Liu B, Wu G, Mao J, et al. 2013. Genesis of the South Asian High and its impact on the Asian summer monsoon onset. J Clim, 26: 2976–2991

Liu J, Kuang X Y, Zhang Y C. 2010. The relationship between the Eastern Hemisphere subtropical westerly jet in the upper troposphere and the subtropical (South Asian) high. Sci Meteorol Sin, 30: 34–41 (in Chinese)

Liu Y, Wu G. 2004. Progress in the study on the formation of the summertime subtropical anticyclone. Adv Atmos Sci, 21: 322–342

Liu Y, Wang Z, Zhuo H, et al. 2017. Two types of summertime heating over Asian large-scale orography and excitation of potential-vorticity forcing. II: Sensible heating over Tibetan–Iranian Plateau. Sci China Earth Sci, 60: 733–744

Nützel M, Dameris M, Garny H. 2016. Movement, drivers and bimodality of the South Asian High. Atmos Chem Phys, 16: 14755–14774

Peng L X, Sun Z B, Chen H S, et al. 2016. Analysis on the multi-center structure of summer South Asia High and its thermal influence factors. Chin J Atmos Sci, 40: 1089–1106 (in Chinese)

Pfister R, Schwarz K A, Janczyk M, et al. 2013. Good things peak in pairs: a note on the bimodality coefficient. Front Psychol, 4: 700

Preacher K J, Hayes A F. 2008. Asymptotic and resampling strategies for assessing and comparing indirect effects in multiple mediator models. Behav Res Methods, 40: 879–891

Qian Y, Zhang Q, Yao Y, et al. 2002. Seasonal variation and heat preference of the South Asia High. Adv Atmos Sci, 19: 821–836

Qu X, Huang G. 2012. An enhanced influence of tropical Indian Ocean on the South Asia High after the late 1970s. J Clim, 25: 6930–6941

Rodwell M J, Hoskins B J. 1996. Monsoons and the dynamics of deserts. Q J R Meteorol Soc, 122: 1385–1404

Schiemann R, Lüthi D, Schär C. 2009. Seasonality and interannual variability of the westerly jet in the Tibetan Plateau region. J Clim, 22: 2940–2957

Siu L W, Bowman K P. 2020. Unsteady vortex behavior in the Asian monsoon anticyclone. J Atmos Sci, 77: 4067–4088

Sobel A H, Nilsson J, Polvani L M. 2001. The weak temperature gradient approximation and balanced tropical moisture waves. J Atmos Sci, 58: 3650–3665

Tao S Y, Zhu F K. 1964. The variation of the 100 hPa flow patterns over southern Asia in summer and its relation to the advance and retreat of the western Pacific subtropical high. Acta Meteorol Sin, 34: 385–396 (in Chinese)

Tyrlis E, Lelieveld J, Steil B. 2013. The summer circulation over the eastern Mediterranean and the Middle East: influence of the South Asian monsoon. Clim Dyn, 40: 1103–1123

Wang J, Li X F, Liu S, et al. 2023. Leading modes of wind field variability over the western Tibet Plateau. Clim Dyn, 60: 1239–1251

Wang J, Li X F, Yang S, et al. 2025. Impact of the Western Tibetan Vortex on springtime snow cover over the western Tibetan Plateau. Geophys Res Lett, 52: e2024GL114453

Wang J, Li X F, Wang J, et al. 2026a. Evaluation of reanalyzed surface air temperature over the western Tibetan Plateau. Atmos Res, 329: 108454

Wang J, Li X F, Wang J, et al. 2026b. Radiative forcing of Western Tibetan Vortex on surface air temperature in spring. Geophys Res Lett, 53: e2025GL119603

Wei W, Zhang R, Wen M, et al. 2015. Interannual variation of the South Asian High and its relation with Indian and East Asian summer monsoon rainfall. J Clim, 28: 2623–2634

Wei W, Zhang R, Wen M, et al. 2017. Relationship between the Asian westerly jet stream and summer rainfall over Central Asia and North China: Roles of the Indian monsoon and the South Asian high. J Clim, 30: 537–552

Wilks D S. 2011. Statistical Methods in the Atmospheric Sciences. 3rd ed. San Diego: Academic Press

Wu G, Liu Y, Zhang Q, et al. 2007. The influence of mechanical and thermal forcing by the Tibetan Plateau on Asian climate. J Hydrometeorol, 8: 770–789

Wu G, Liu Y, He B, et al. 2012. Thermal controls on the Asian summer monsoon. Sci Rep, 2: 404

Xie S P, Hu K, Hafner J, et al. 2009. Indian Ocean capacitor effect on Indo–western Pacific climate during the summer following El Niño. J Clim, 22: 730–747

Xue X, Chen W, Chen S, et al. 2015. Modulation of the connection between boreal winter ENSO and the South Asian high in the following summer by the stratospheric quasi-biennial oscillation. J Geophys Res-Atmos, 120: 7393–7411

Yang J, Liu Q, Xie S P, et al. 2007. Impact of the Indian Ocean SST basin mode on the Asian summer monsoon. Geophys Res Lett, 34: L02708

Zarrin A, Ghaemi H, Azadi M, et al. 2011. The effect of the Zagros Mountains on the formation and maintenance of the Iran Anticyclone using RegCM4. Meteorol Atmos Phys, 112: 91–100

Zhang P, Liu Y, He B. 2016. Impact of East Asian summer monsoon heating on the interannual variation of the South Asian High. J Clim, 29: 159–173

Zhang Q, Wu G X. 2001. The large area flood and drought over Yangtze River valley and its relation to the South Asia High. Acta Meteorol Sin, 59: 569–577 (in Chinese)

Zhang Q, Wu G, Qian Y. 2002. The bimodality of the 100 hPa South Asia High and its relationship to the climate anomaly over East Asia in summer. J Meteorol Soc Jpn, 80: 733–744

Zhou B, Hu S, He Y, et al. 2022. Quantitative evaluations of subtropical westerly jet simulations over East Asia based on multiple CMIP5 and CMIP6 GCMs. Atmos Res, 276: 106257

Supplementary Files

This is a list of supplementary files associated with this preprint. Click to download.

- supplementary.docx